Crack Identification of a Rotating Shaft With Integrated Wireless Sensors

By

Fernando Andrés Bejarano Rodríguez

A thesis submitted in partial fulfillment of the requirements for the degree of

MASTER OF SCIENCES

in

MECHANICAL ENGINEERING

UNIVERSITY OF PUERTO RICO

MAYAGÜEZ CAMPUS

2007

Approved by:

_____
Frederick Just, PhD
Member, Graduate Committee — Date

_____
David Serrano, ScD
Member, Graduate Committee — Date

_____
Yi Jia, PhD
President, Graduate Committee — Date

_____
Pedro Resto, PhD
Representative of Graduate Studies — Date

_____
Paul Sundaram, PhD
Chairperson of the Department — Date

Abstract

This study developed a novel real-time monitoring diagnostic method of determining the position and depth of a transverse open crack on a rotating shaft, which vibrates in bending due to the harmonic excitation force induced by an unbalanced disk coupled at the midspan.

The development of a new wireless sensor capable of being mounted directly on the shaft allowed modeling of the dynamic system using the data obtained at different points of interest of the structure in the rotating coordinate system.

Vibration parameters were obtained first from a simulation employing the Finite Element Method and then experimentally using Modal Analysis for different crack positions and depths. The unique relation between the vibration parameters and crack characteristics found was employed to solve the inverse problem; relate failure patterns of acceleration at different points of the shaft with the crack size and location by means of Artificial Neural Networks Method working as function approximator.

The predictive neural networks were selected experimentally and then validated showing that the damage detection sensitivity parameters used depended on the acceleration signals at different points of the shaft.

Resumen

Este estudio desarrolló un nuevo método de monitoreo en tiempo real de la posición y profundidad de una fractura transversal abierta en un eje en rotación, el cual vibra en flexión debido a la fuerza de excitación inducida por un disco desbalanceado acoplado en el medio. El desarrollo de un nuevo sensor permitió realizar el análisis dinámico en coordenadas rotacionales mediante la obtención de parámetros de vibración en diferentes puntos de interés del eje.

Los parámetros de vibración fueron obtenidos primero por una simulación empleando el Método de Elementos Finitos y luego experimentalmente usando Análisis Modal para diferentes posiciones y profundidades de fractura. La relación única encontrada entre los parámetros de vibración y las características de la fractura fue empleada para resolver el problema inverso; relacionar patrones de falla de aceleraciones en diferentes puntos del eje con el tamaño y la localización de la fractura mediante el método de Redes Neuronales Artificiales trabajando como aproximador de funciones.

Las redes neuronales predictivas fueron seleccionadas experimentalmente y luego validadas mostrando que los parámetros de sensitividad de falla utilizados dependieron de las señales de aceleración en diferentes puntos del eje.

Dedications

To my family, for the constant support, for being my inspiration and my biggest treasure. To my beloved Paito who give me the force to all the projects of my life. To my first pretty niece Gabriela, who was born in the moment I finished this research. To my closest friends who always remain with me regardless the time and distance. To this amazing planet earth, marvel of God, by which I will always do my best to construct a better place to live.

Acknowledgments

I would like to take this opportunity to express my sincere gratitude to Professor Dr. Yi Jia for his constant guidance, support and valuable advice throughout this research and my Master's studies in general. I also would like to thank the members of my committee: Dr. Frederick Just and Dr. David Serrano for dedicating time to providing valuable ideas on this work.

The author would like to thank the Mechanical Engineering Department of the University of Puerto Rico for giving me the opportunity of pursuing my graduate studies and providing economic assistance during my graduate studies. I am grateful to National Science Foundation and Department of Energy for the support of this research under grant 0549338 and DE-FG26-07NT43061.

Particular thanks are due to Paola Hernandez, Luis Quintero and Sun Ke, who provided valuable assistance in this project. Thank you all for your kindness and friendship.

Finally, I would like to thank my family for their constant support and good energy given during my graduate studies.

Table of Contents

Abstract ii

Resumen iii

Dedications iv

Acknowledgments v

Table of Contents vi

List of Figures ix

List of Tables xi

Index of Symbols xii

1 Introduction 1

1.1 Objectives 2

2 Literature Review 3

2.1 Model Based Methods 3

2.2 Experimental Methods 6

2.3 Overall Approach 9

2.4 General Description of the System 10

3 Mathematical Modeling of the Dynamic System 11

3.1 Derivation of the Harmonic Force 11

3.2 Dynamic Analysis of the Uncracked Shaft in Forced Flexural Vibration 17

3.2.1 Solution of the Equation of Motion in Free Vibration 18

3.2.2 Eigen Value Problem for the Shaft with Both Ends Fixed 19

3.2.3 Eigen Values Estimation 20

3.2.4 Mode Shapes of the Shaft with Fixed Ends 21

3.2.5 Shaft under Forced Vibration 22

3.3 Random Signal Analysis *27*

3.4 Conclusions *29*

4 Finite Element Model of the Rotating Cracked Shaft 30

4.1 Derivation of the Element Stiffness Matrix *31*

4.2 Derivation of the Consistent Element Mass Matrix *35*

4.3 Reduction of Dynamic Global Matrices *35*

4.3.1 Assembly of the System Stiffness Matrix 36

4.3.2 System Mass Matrix 37

4.3.2.1 Eigen Values Estimation 39

4.3.2.2 Modal Shapes Estimation 39

4.3.2.3 Modal Matrix Assemble 40

4.4 The Steady State Response Estimation *40*

4.5 Results from the Finite Element Model *41*

4.5.1 Changes of the Vibration Parameters 41

5 Identification of Crack Size and Location Based on Neural Networks Method 46

5.1.1 Assemble of the training data 47

5.1.2 Creation of the Neural Network Object 48

6 Experimental Study 53

6.1 Signal Processing *53*

6.1.1 The Fast Fourier Transform 53

6.1.2 Errors 54

6.1.2.1 Aliasing 54

6.1.2.2 Leakage 55

6.2 Wireless Sensor Development *55*

6.2.1 Circuit Design Process 56

6.2.2 Exposing the Pre-sensitized P.C.B 57

6.2.3 Developing 57

6.2.4 Etching 57

6.2.5 Soldering the Circuit 57

6.2.6 Sensitivity of the wireless sensor 58

6.2.7 Data Acquisition System and Experimental Setup 59

6.3 Experimental Results *60*

6.4 Comparison between theoretical and experimental results *64*

7 Results and conclusions 65

8 Future Work 68

References 69

List of Figures

Figure 1. Overall Scheme of the Crack Diagnostic Approach 9
Figure 2. (a) Pelton drawing (www.newmillshydro.com) (b) The Jeffcott Rotor 10
Figure 3 (a) Simplified System Scheme (b) Section of the unbalanced disk 11
Figure 4. Vectorial triangle 14
Figure 5. Free body diagram of a simplified SDOF system 15
Figure 6. Maximum Deflection in the Middle of the Shaft 16
Figure 7. Shaft in forced vibration – Generalized case 17
Figure 8. Eigen values estimated graphically 20
Figure 9. First mode shape of the uncracked shaft 21
Figure 10. Second mode shape of the uncracked shaft 22
Figure 11. Third mode shape of the uncracked shaft 22
Figure 12. Deflection of the shaft at different times 27
Figure 13. PSD Acceleration Amplitudes at different position of the shaft rotating at 4 Hz 28
Figure 14. Cracked Shaft Model 30
Figure 15. Euler Bernoulli Beam Finite Element 31
Figure 16. Static deflection curves due to unit displacement at nodal coordinate 1 32
Figure 17. Fixed shaft divided in six elements and its nodal coordinates 36
Figure 18 Second moments of inertia of the cracked and uncracked shaft 36
Figure 19. Change in frequency for different crack depths and positions (a) First harmonic (b) Frequency difference between cracked and uncracked shaft 42
Figure 20. Mode Shapes of the shaft with crack depth =4.76 mm, crack position =140 mm 42
Figure 21. Amplitude of acceleration at the nodal coordinates of the shaft with crack depth =4.76 mm at 4.8 Hz driving frequency (a) crack position=76 mm (b) crack position =140 mm 43
Figure 22. Acceleration of the shaft at node 4 with crack depth =4.76 mm and a driving frequency of 4.8 Hz (a) crack position=76 mm (b) crack position =140 mm 43
Figure 23 PSD of acceleration signals at node 4 for the shaft with crack depth =4.76 mm and driving frequency of 4.8 Hz (a) Crack at 76 mm (b) Crack at 140 mm 44
Figure 24 Difference in PSD-Amplitudes of acceleration for (a) Different crack positions (b) Different crack depths 44
Figure 25 Response Surfaces of the Power Spectral Density Difference between Cracked and Uncracked shaft (a) Node 4 and (b) Node 5 45
Figure 26. Training data sets: Inputs = (amplitudes of acceleration frequency response at nodes 4, 5 and 6, and Outputs = (crack positions and depths) 48
Figure 27. Predicted average error from simulated data (a) Crack position with a sigmoidal transfer function (b) Crack depth with sigmoidal transfer function 50

Figure 28. Predicted average error from simulated data (c) Crack position with a hyperbolic tangent function (d) Crack depth with a hyperbolic tangent function 50
Figure 29. Predicted average error from simulated data (e) Predicted total error with Sigmoidal transfer function (f) Predicted total error with Hyperbolic tangent transfer function.....50
Figure 30. Neural network structure for the predictive model with simulated data.....51
Figure 31. Performance of the network predictor (a) Crack positions (b) Crack depths 52
Figure 32. Representation of the Accelerometer and duty cycle [3] (a) Accelerometer (b) Analog duty cycle signal56
Figure 33. (a) Circuit designs for the PCB (b) Accelerometer block diagram taken from [3].....57
Figure 34 (a) Accelerometer and transmitter circuits (b) Receiver circuit 58
Figure 35. Data Acquisition System and Experimental Setup.....59
Figure 36. Signal processing (a) Duty Cycle Signal (b) Acceleration Signal in the time.....60
Figure 37. (a) Acceleration filtered signal (b) Acceleration Power Spectral Density.....60
Figure 38. Experimental power spectral density amplitude differences 61
Figure 39. Predicted average error from experimental data (a) Crack position with a sigmoidal transfer function (b) Crack depth with sigmoidal transfer function 62
Figure 40. Predicted average error from experimental data (c) Crack position with a hyperbolic tangent function (d) crack depth with a hyperbolic tangent function 62
Figure 41. Predicted average error from experimental data (e) Total error with sigmoidal transfer function (f) Total error with hyperbolic tangent transfer function.....62
Figure 42. Neural network structure schematic for the predictive model for the experimental data 63
Figure 43. Performance of the predictor network (a) Crack positions (b) Crack depths 63

List of Tables

Table 1. Properties of the Shaft and the Disk 10
Table 2. Simulation Data Sets 41
Table 3. Analysis of variance for the Total Error of the simulated data 49
Table 4. Performance of the neural network for the simulating data 52
Table 5. Analysis of variance for the Total Error of the experimental data 61
Table 6. Performance of the neural network for experimental data 64
Table 7. Comparison between theoretical and experimental PSDA 64
Table 8. Comparison between theoretical and experimental predicted data 64

Index of Symbols

X, Y - General Coordinates

i, j - Rotating Coordinates

t - Time in [seconds]

g - Gravity [m/s^2]

E - Modulus of elasticity [N/m^2]

e - Eccentricity [mm]

ω - Driving frequency in [Hz]

ω_n - Natural frequency in [Hz]

θ - Rotating angle [radians]

m - Mass [Kg]

$\bar{m}$ - Mass per unit length [Kg/mm]

ρ - Specific mass [Kg/m^3]

r - Radius of the shaft [mm]

A - Cross sectional area [mm^2]

I - Moment of inertia [mm^4]

L -Length of the shaft [mm]

l - Length of the finite element [mm]

c - Damping factor [N-seg/m]

ξ - Damping ratio

K - Stiffness [N/m]

ϕ - Phase angle [radians]

τ - Period [seconds]

PSD - Power Spectral Density [g^2/Hz]

PSDAA - Power Spectral Density Amplitude of Acceleration [g^2/Hz]

a - Array of neuron output

W - Array of connection weights

b - Array of biases

f - Transfer function

s - Sensitivity

$\dot{F}$ - Jacobian

k - Iteration number

α - Learning rate

1 Introduction

Rotating shafts carrying disks are broadly used in many mechanical applications like pumps, engines and turbines. It is observed that high speed and heavy duty shafts develop transverse cross-sectional cracks due to fatigue at some time during their life period. Cracks may be caused by mechanical stress raisers, such as sharp keyways, abrupt cross sectional changes, metallurgical factors, heavy shrink fits, grooves, and other stress concentration factors that promote the crack initiation.

Once a crack is initiated it propagates and the stress required for propagation is smaller than that required for crack initiation. After many cycles operating stresses may be sufficient to propagate the crack. The crack propagation takes place over a certain depth when it is sufficient to create unstable conditions and fracture take place. It is important to develop new non-destructive techniques real time based diagnosis methods to predict the behavior of a crack in order to avoid human and economical disasters.

Transverse cracks modifies the dynamic behavior of the system generating in an horizontal shaft a reduction of the rotor stiffness, which change the modal parameters and the acceleration amplitudes along the shaft. Establishing a relation between these vibration parameters and the failure characteristics of the system will leave us to characterize and predict a failure in a rotor system. This research developed a novel real time monitoring method based artificial neural networks method working as a function approximator to predict the crack location and size of a rotating shaft by using wireless sensor technology directly mounted on the shaft.

Monitoring techniques to detect transversal cracks in rotating mechanical shafts during operation are necessary, since the conventional NDT techniques such as ultrasonic, dye penetrants or magnetic particles require the equipment to be taken out of service for some period of time. Vibration analysis with proximity sensors like eddy current, requires them to be mounted on special fixtures that should be fixed close to the rotor structure, therefore the shaft should be dismounted from the operation place.

Mounting wireless sensors directly on the shaft permits to get vibration parameters in specific points of the rotating shaft without the need of dismounting the shaft. Using wireless

accelerometers allows greater amplitudes of vibration than the conventional methods like eddy current proximity sensors, where the distance between the rotating shaft and the proximity sensor is limited.

Machinery diagnostics for maintenance of a structure or machine can be done using wireless accelerometers by monitoring its amplitudes of frequency response. A shift in the acceleration pattern or some other parameter will indicate a pending failure that could happen in the presence of a crack.

Different types of rotating components like eccentric parts which lead to unbalanced rotor systems like crankshafts, cams and linkages, etc could be monitored by employing wireless accelerometers for modal analysis. Knowing the crack location and size, a future forecasting method can estimate the residual amount of time left in the shaft based on past and current states.

1.1 Objectives

In order to fulfill the development of a new wireless sensor and the online prediction model to detect the location and size of a transverse crack on a rotating shaft, the following specific tasks are required:

Simulate the dynamic system and extract the vibration parameters from a cracked and uncracked shaft by means of Finite Element Analysis.

Apply a Neural Network Model to correlate vibration signals with crack positions and depths for the theoretical and experimental data.

Design and fabricate a new wireless accelerometer capable of obtaining the vibration signal of a rotating shaft and converting it to digital signal for further processing.

Predict the response of the system employing signal processing techniques to extract the vibration parameters of the cracked and uncracked shafts.

Carry out design of experiments to select the best architecture used as network predictor and compare the experimental and analytical models employed for the crack characterization.

2 Literature Review

Literature on crack detection and diagnostics was focused on the vibration-based method technique, which can be classified into signal-based and model-based methods.

Model-based methods are based on analytical or numerical models to simulate the behavior of cracked shafts during operation and attempt to correlate the observed vibration signature with the presence of a crack at discrete locations on the shaft.

Experimental-based methods commonly employ vibration monitoring equipment (such as proximity probes, phase reference, and spectrum analyzers) with or without additional systems, such as torsional vibration measurement, etc. Steady-state and/or transient vibration data are analyzed for known indicators of cracks.

2.1 Model Based Methods

In 1976, I.W. Mayes and W.G. Davis [17] stated that the crack in a shaft could be theoretically modeled using the virtual work principle, by applying the conservation of energy to describe the crack behavior. The stress distribution and the bending moment around the area of the crack were needed in order to perform this approach. It was found that the equations of motion for the system are nonlinear, due to the unbalanced forces acting on the crack.

The theory showed that the response due to a crack may be zero, or unbalanced by 180 degrees out of phase with the crack. In addition, it was shown that the response due to the crack is the same as if one would add an extra unbalanced force of predetermined magnitude and angle to the original unbalance.

Mayes in 1984 utilized standard linear rotor dynamics response programs to solve the typical rotor dynamics equation, where the coordinates are in a fixed coordinate system in space and the change in the shaft stiffness matrix appeared as an applied external sinusoidal force to the system. This applied external sinusoidal force was found to be a function of the change in the area moment of inertia of the rotor as a result of the crack, as well as the rotating axis respect to the fixed coordinate system.

In 1983 Dimarogonas [17] analyzed a Laval rotor system, and modeled the breathing effect of a crack using bi-linear and analytical methods for an open crack. As a result, crack flexibility functions for the rotor were developed. In addition, with the assumption that the shaft undergoes large static deflections, the crack flexibility matrix was obtained for a closed crack. Finally, Dimarogonas created a flexibility function based on empirical data in the form of a truncated Fourier series.

Petroski, Papadopoulos and Dimarogonas (1987, 1988, 1992) [2] published a series of papers on rotating and non-rotating shafts with an open crack. They derived a local flexibility matrix that depends on the crack depth. The no diagonal terms of this matrix cause coupling between the longitudinal, torsional, and bending vibrations. The stiffness of the system depends on the crack depth and the slenderness of rotating shaft during passage through a critical speed.

Narkis Y. in 1992 [18] derived a continuous equation to determine the location of a crack on a homogeneous, symmetric rotor. The location of the crack was determined to be one of two places, since the equation's location is symmetric from the middle of the rotor. The crack was simulated by an equivalent spring, connecting the two segments of the beam.

Narkis used algebraic equations which relate natural frequencies to beam and crack characteristics. It was found that the only information required for accurate crack identification is the variation of the first two natural frequencies due to the crack. The reliability of the proposed method was evaluated with finite element method using ANSYS software giving acceptable results, however the side were the crack was located was not uniquely defined by this method.

Sekhar in 2001 [22] studied a method based on online identification of cracks in a rotor while it is passing through its flexural critical speed. The fault induced change of the rotor system was taken into account by equivalent loads in a mathematical model.

The equivalent loads are virtual forces and moments acting on the linear undamaged system to generate a dynamic behavior identical to the measured one of the damaged system. The rotor was modeled using FEM, while the crack is considered through local flexibility change.

The crack was identified for its depth and location on the shaft for different rotor accelerations. The nature and symptoms of the fault crack are further ascertained using continuous wavelet transform.

Bikri K. El, Benamar R. and Bennouna M.M. in 2006 [5] performed a theoretical investigation of the geometrically non-linear free vibrations of a clamped–clamped beam containing an open crack. The approach used a semi-analytical model based on an extension of the Rayleigh–Ritz method to non-linear vibrations, which is mainly influenced by the choice of the admissible functions.

The general formulation was established using new admissible functions, called ‘‘cracked beam functions’’, and denoted as ‘‘CBF’’, which satisfy the natural and geometrical end conditions, as well as the inner boundary conditions at the crack location.

Iterative solution of a set of non-linear algebraic equations was obtained numerically, which leads to the basic function contribution coefficients to the displacement response function. Then, an explicit solution is derived and proposed as an alternative procedure, simple and ready to use for engineering applications.

Emphasis was made on the backbone curves, i.e. amplitude-frequency dependence, obtained for various crack depth, and the effect of the vibration amplitudes upon the non-linear mode shapes of a cracked beam was examined. The work was restricted to the fundamental mode in order to concentrate on the study of the influence of the crack on the non-linear dynamic response near to the fundamental resonance.

Most of the literature review on model based methods treated the problem of crack identification analyzing the system in the static frame of coordinates to estimate the changes in natural frequencies, mode shapes and damping ratios of the shaft due to a reduction in local stiffness provoked by the presence of a crack. These methods require enormous amounts of computational time and effort. Furthermore, it is not easy to obtain an accurate measure of the crack effects using an analytical approach.

The simulating study presented in this thesis introduces the analysis of the dynamic system in the rotating coordinates based on the failure pattern of acceleration signals at different points of the shaft rotating at a constant driving frequency.

2.2 Experimental Methods

Gasch in 1976 [25] studied the stability behavior of the Laval rotor with a crack, and the forced vibration due to imbalance and crack. He replaced the crack mechanism by an additional flexibility and switched it on and off according to whether the crack was closed or open. The results showed that the recognition of cracks is very difficult because the significant double and triple frequency vibration are only very slightly involved in the crack response.

Grabowski B. in 1980 [1][12] used modal analysis to study the vibration behavior of a turbine rotor containing a transverse crack. His results showed that a crack causes important changes in shaft vibration. He reported that the crack excites 1X and 2X vibrations, which are independent of the out of balance but depend on the crack locations.

Tsai T. C. And Wang Y. Z. in 1996 [24] studied a diagnostic method of determining the position and size of a transverse open crack on a stationary shaft without disengaging it from the machine. The crack was modeled as a joint of a local spring. To obtain the dynamic characteristics of a stepped shaft and a multi-disc shaft, the transfer matrix method was employed on the basis of Timoshenko beam theory.

The simplest model of the so-called Laval rotor, which is an elastic but mass-less shaft with an unbalanced disc and an always open transverse crack was taken to provide an equation of motion for a cracked shaft, enabling to estimate the natural frequencies, amplitudes of forced vibrations and areas of dynamic stability change related to the crack conditions at various rotational speeds.

The open crack is regarded as a local spring with a constant value that is derived from the relationship between the strain energy and stress intensity factor in fracture mechanics. Crack positions were identified from comparing the fundamental mode shapes of the shaft with and without crack and the depth was obtained by the change of natural frequency of the shaft with and without a crack.

Experiments were conduced with a impact test carried out with a signal processing apparatus composed by a dual channel spectrum analyzer, a hammer, an accelerometer and a charge amplifier. The investigation presented excellent results in crack position identification.

Feldman and Seibold in 1998 [10] used the Hilbert transform (HT) to detect non-linearity's from the measured vibration of a rotor. The HT converts the signal into a slowly-varying envelope type signal and a phase angle. Basic vibration data, such as stiffness, system damping, etc., can be deduced from this. Identification algorithms, based on the extended Kalman filter (EKF) and the instrumental variables method can then be applied to the transformed data to detect cracks.

The EKF is a time domain identification algorithm and Seibold and Weinert show that the depth of the crack can be calculated correctly, even if the measurement information is incomplete. The localization is performed by designing a bank of EKFs, in which each filter is tuned to a different damage hypothesis, i.e. in this case the specific crack location. By calculating the probabilities of the different hypotheses, the crack can be localized and its depth can be determined.

Owolabi G. M. in 2002 [19] studied the vibration behavior of aluminum beams based on changes in the natural frequencies and amplitudes of the FRFs. Galerkin's method was utilized to solve for the frequencies and vibration modes in a simulating model. Modal analysis was performed in the experimental work employing a dual channel signal analyzer and seven light accelerometers placed at different points of the beam. Results have shown that vibration behavior of the beams are very sensitive to the crack location, crack depth and mode number.

This study illustrates that measured parameters of frequencies and response amplitudes are unique values, which remain the same (within a tolerance range), whether similar beams are tested and responses measured. The unique values of the crack location and crack depth were obtained by plotting the contour lines of the first three modes of the fixed beam.

Fan Yimin and Li C. James in 2000 [9] used an embedded modeling approach to identify the change in stiffness of a shaft as a result of a crack. They worked with a new methodology to identify multi-degree of freedom nonlinear systems from the system's operating data.

The methodology includes a new nonlinear model architecture which embeds feedforward neural networks to represent unknown nonlinearities in a lumped parameter model, and a learning

algorithm to train the embedded neural networks as well as model parameters to obtain model fidelity. The change in stiffness of the shaft was approximated using neural network, which is then, in turn, embedded in a lumped parameter model of the shaft.

The neural network is refined iteratively with a solution method to minimize a cost function based on the difference in the response of an embedded model and the data collected from the cracked system. The finite element model used was basically a two-dimensional one in the XZ plane and in the YZ plane, where Z is the longitudinal axis of the shaft. The procedure was applied to a simulated rotor and also to a test rig.

Sinha Jyoti K. in 2006 [23] used bi-spectrum tool in the signal processing for identification of non-linear dynamic behavior. This investigation shows breathing of a crack during shaft rotation also on a non-linear behavior. The bi-spectrum results are found to be encouraging to distinguish the faults based on few experiments conducted on a small experimental rig.

The crack and the misalignment in the shaft is detected and distinguished using orbit plots during machine transient operation (run-up or run-down) though both the faults generate higher harmonics in the shaft responses. Measurements in both the vertical and horizontal directions on a fixed ware frame were required.

In this research, an attempt has been made to detect the presence of a crack in a rotating shaft, and determine its location and size, based on experimental modal analysis. Previews experimental methods require high speeds to extract modal parameters like natural frequencies and frequency response amplitudes.

The advantage of the proposed method is that the system can be safety monitored online without the need to reach the fundamental frequency avoiding extreme operational conditions for diagnosis. Besides the crack can be identified and characterized in operational condition without the need of dismounting the shaft.

2.3 Overall Approach

This work presents a novel real time monitoring technology which relates a set of frequency response amplitudes of acceleration of a shaft rotating at a fixed driving frequency with different crack positions and depths.

A fault simulator machine is employed to simulate the system, where a shaft is supported on two bearings and a disk is attached at the midspan. The shaft is rotated by an electrical motor coupled to the shaft on one side. The rotating shaft vibrates in bending due to the harmonic excitation force induced by the unbalanced disk. Overall of this study is explained as follows:

The simulating study begins with the analytical derivation of the ordinary differential equation that describes the vibrating system. Modal parameters were calculated for an uncracked shaft employing separation of variables method.

Finite element method was used to calculate the modal parameters of the cracked shaft for known crack depths and positions. Then the best artificial neural network trained with Backpropagation algorithm is found from a design of experiment to solve the inverse problem: from the modal parameters estimate the crack characteristics.

The experimental study starts with the wireless accelerometer development, and then, signals conditioning and signal processing is applied to the signal to obtain the acceleration signal in the radial direction of the shaft for three different points. Finally the best diagnostic network is selected to associate the acceleration signal with the crack depth and position.

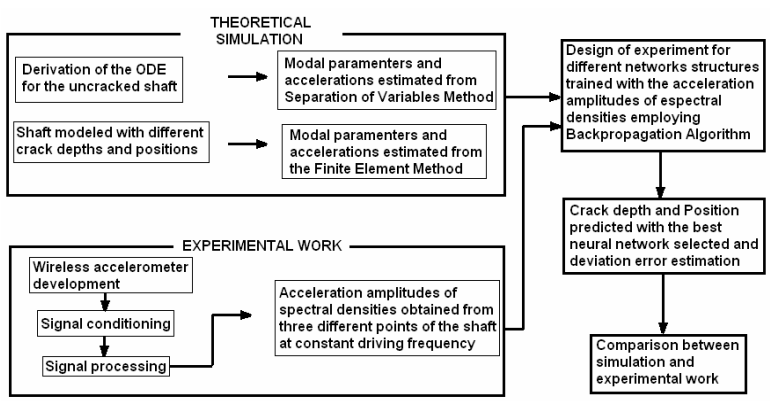

Figure 1. Overall Scheme of the Crack Diagnostic Approach

2.4 General Description of the System

A complex system like a Pelton turbine similar to that shown in the Figure 2(a) can be represented by a Jeffcott Rotor in Figure 2 (b), where the rotating shaft-disk system is modeled assuming that the bearings are rigid and provide no damping to the system. The shaft is assumed to be elastic and will deflect with respect to its equilibrium position in the presence of external mass unbalance due to the eccentricity of a rigid circular disk mounted at the midspan.

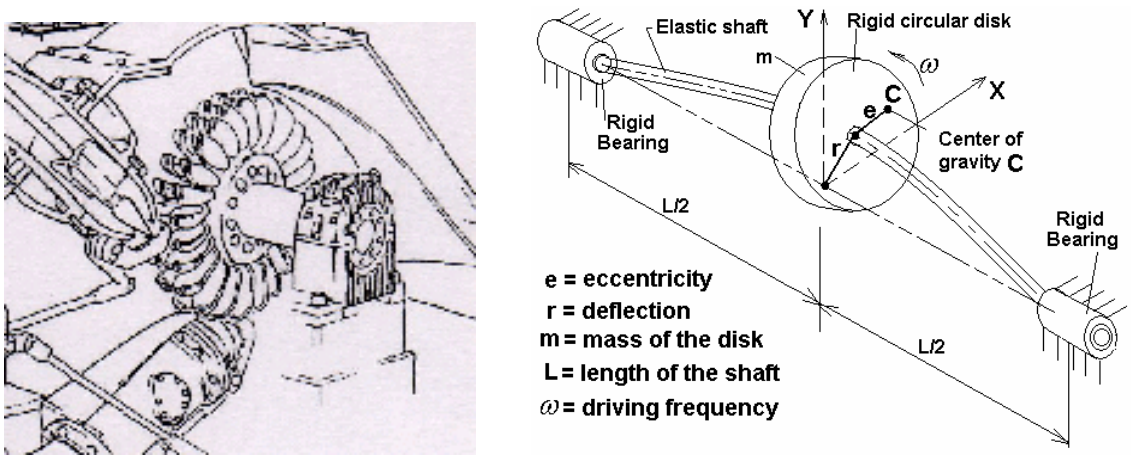

(a) (b)

Figure 2. (a) Pelton drawing (www.newmillshydro.com) (b) The Jeffcott Rotor

A slender plastic shaft was selected with a heavy steel disk in order to vibrate the system at low frequencies in the experimental work. A driving frequency ω = 4.8 Hz and an eccentricity of 1.2 mm were selected for the simulation study. The properties of the shaft and the disk are summarized in the following table:

Table 1. Properties of the Shaft and the Disk

SHAFT					DISK			
Material	Diameter [mm]	Length [mm]	Density [g/cc]	Young's Modulus "E" [Mpa]	Material	Diameter [mm]	Width[mm]	Weight [Kg]
Acetal Delrin (Homopolymer)	9.53	330.20	1.41	3103.45	Steel AISI 10	101.6	15.9	7.76

3 Mathematical Modeling of the Dynamic System

Understanding the dynamic behavior of the uncracked rotating shaft harmonically excited by an unbalance disk is the first step before modeling the cracked shaft scenario. The system was analyzed in the rotating system of coordinates because the wireless sensor developed rotates attached to the shaft.

First the harmonic force of the unbalanced disk was derived in a reduced two degrees of freedom system; r and θ, to a single degree of freedom in the radial direction of the shaft. Then a continuous shaft with harmonic force acting in the middle was analyzed.

The shaft was modeled mathematically using mechanics of materials principles based on the Euler Bernoulli theory to derive the partial differential equations that describe the uncracked vibrating shaft. Then the method of separation of variables was employed to solve the eigen value problem in order to find the vibration parameters such as: natural frequencies, mode shape functions, displacement and acceleration equations.

3.1 Derivation of the Harmonic Force

The analysis of the harmonic force F(ωt) induced by the unbalance rotating disk is done by taking the section of the rotating disk as shown in Figure 3(a) and (b) :

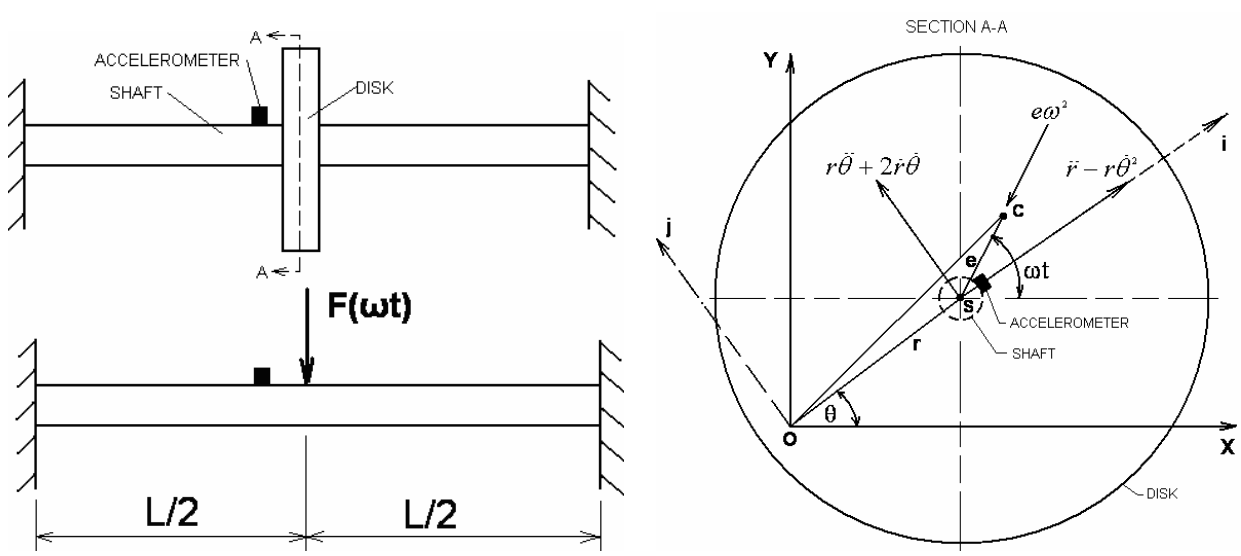

(a) (b)

Figure 3 (a) Simplified System Scheme (b) Section of the unbalanced disk

O is the rotating center and origin of the inertial system X, Y. The center of the disk-mass is C, which is at a distance e (eccentricity) from the geometrical center of the disk at S. The disk is rotating at a constant driving frequency ω with a deflection r.

The vectors of motion involving the mass center C are calculated as:

$$\begin{array}{lll} \textit{Position} & \textit{Velocity} & \textit{Acceleration} \\ \vec{p}_c = \vec{p}_s + \vec{p}_{c/s} & \vec{v}_c = \vec{v}_s + \vec{v}_{c/s} & \vec{a}_c = \vec{a}_s + \vec{a}_{c/s} \end{array} \quad \textbf{(1)}$$

Position, velocity and acceleration vector components of point S in the fixed coordinate system ''X'' and ''Y'' are:

$$\begin{aligned} \textit{Position}: \quad & X_s = r\cos\theta \\ & Y_s = r\sin\theta \\ \textit{Velocity}: \quad & \dot{X}_s = \dot{r}\cos\theta - r\dot{\theta}\sin\theta \\ & \dot{Y}_s = \dot{r}\sin\theta + r\dot{\theta}\sin\theta \\ \textit{Acceleration}: \quad & \ddot{X}_s = [\ddot{r} - r\dot{\theta}^2]\cos\theta - [2\dot{r}\dot{\theta} + r\ddot{\theta}]\sin\theta \\ & \ddot{Y}_s = [2\dot{r}\dot{\theta} + r\ddot{\theta}]\cos\theta + [\ddot{r} - r\dot{\theta}^2]\sin\theta \end{aligned} \quad \textbf{(2)}$$

Translating velocities and accelerations into the rotating coordinate system ''$\overline{r}$'' and ''$\overline{\theta}$''gives:

$$\begin{aligned} \textit{Velocity}: \; V_{Si} &= \dot{X}_S\cos\theta + \dot{Y}_S\sin\theta \\ &= \dot{r}\cos^2\theta - r\dot{\theta}\sin\theta\cos\theta + \dot{r}\sin^2\theta + r\dot{\theta}\cos\theta\sin\theta = \dot{r} \\ V_{Sj} &= \dot{Y}_S\cos\theta - \dot{X}_S\sin\theta \\ &= \dot{r}\sin\theta\cos\theta + r\dot{\theta}\cos^2\theta - \dot{r}\cos\theta\sin\theta + r\dot{\theta}\sin^2\theta = r\theta \end{aligned} \quad \textbf{(3)}$$

$$\begin{aligned} \textit{Acceleration}: a_{Si} &= \ddot{X}\cos\theta + \ddot{Y}\sin\theta \\ &= [\ddot{r} - \dot{r}\dot{\theta}^2]\cos^2\theta - [2\dot{r}\dot{\theta} + r\ddot{\theta}]\sin\theta\cos\theta + [2\dot{r}\dot{\theta} + r\ddot{\theta}]\cos\theta\sin\theta \\ &\quad + [\ddot{r} - r\dot{\theta}^2]\sin^2\theta = [\ddot{r} - r\dot{\theta}^2][\cos^2\theta + \sin^2\theta] = \ddot{r} - r\dot{\theta}^2 \\ a_{Sj} &= -\ddot{X}\sin\theta + \ddot{Y}\cos\theta \\ &= -[\ddot{r} - r\dot{\theta}^2]\cos\theta\sin\theta + [2\dot{r}\dot{\theta} + r\ddot{\theta}]\sin^2\theta + [2\dot{r}\dot{\theta} + r\ddot{\theta}]\cos^2\theta \\ &\quad + [\ddot{r} - r\dot{\theta}^2]\sin\theta\cos\theta = [2\dot{r}\dot{\theta} + r\ddot{\theta}][\sin^2\theta + \cos^2\theta] = 2\dot{r}\dot{\theta} + r\ddot{\theta} \end{aligned} \quad \textbf{(4)}$$

Relative accelerations of the center of gravity of the disk at C with respect to the center of the disk $a_{C/S}$ in the rotating coordinates are derived as follows:

$$\begin{aligned}
&Position: && X_{C/S} = e\cos(\omega t), && Y_{C/S} = e\sin(\omega t) \\
&Velocity: && \dot{X}_{C/S} = -e\omega\sin(\omega t), && \dot{Y}_{C/S} = e\omega\cos(\omega t) \\
&Acceleration: && \ddot{X}_{C/S} = -e\omega^2\cos(\omega t), && \ddot{Y}_{C/S} = -e\omega^2\sin(\omega t)
\end{aligned} \tag{5}$$

Translating the accelerations into the rotating coordinate system ''$\bar{r}$'' and ''$\bar{\theta}$'' we have:

$$\begin{aligned}
a_{(C/S)i} &= \ddot{X}_{(C/S)}\cos\theta + \ddot{Y}_{(C/S)}\sin\theta \\
&= -e\omega^2\cos(\omega t)\cos(\theta) - e\omega^2\sin(\omega t)\sin(\theta) = -e\omega^2\cos(\omega t - \theta) \\
a_{(C/S)j} &= \ddot{X}_{(C/S)}\sin\theta + \ddot{Y}_{(C/S)}\cos\theta \\
&= -e\omega^2\cos(\omega t)\sin(\theta) - e\omega^2\sin(\omega t)\cos(\theta) = -e\omega^2\sin(\omega t - \theta)
\end{aligned} \tag{6}$$

Replacing terms from equations (4) and (6) in equation (1) for the accelerations of the center of gravity a_C of the disk in the radial and tangential direction gives:

$$\begin{aligned}
a_{Ci} &= \ddot{r} - r\dot{\theta}^2 - e\omega^2\cos(\omega t - \theta) \\
a_{Cj} &= 2\dot{r}\dot{\theta} + r\ddot{\theta} - e\omega^2\sin(\omega t - \theta)
\end{aligned} \tag{7}$$

Applying Newton's second law the equations of motion resolved in the radial and tangential directions become:

$$-Kr - c\dot{r} = m_d[\ddot{r} - r\dot{\theta}^2 - e\omega^2\cos(\omega t - \theta)] \tag{8}$$

$$-cr\dot{\theta} = m_d[r\ddot{\theta} + 2\dot{r}\dot{\theta} - e\omega^2\sin(\omega t - \theta) \tag{9}$$

Last two equations can be rearranged

$$\ddot{r} + \frac{c}{m_d}\dot{r} + (\frac{k}{m_d} - \dot{\theta}^2)r = e\omega^2\cos\left(\omega t - \theta\right) \tag{10}$$

$$r\ddot{\theta} + (\frac{c}{m_d}r + 2\dot{r})\dot{\theta} = e\omega^2\sin\left(\omega t - \theta\right) \tag{11}$$

From the right part of equation (10) we get the harmonic force in the sensor sensitivity direction:

$$F(\omega t) = m_d e\omega^2 \cos(\omega t - \theta) \tag{12}$$

In steady state synchronous whirl we have

$$\dot{\theta} = \omega \quad and \quad \ddot{\theta} = \ddot{r} = \dot{r} = 0 \tag{13}$$

Integrating we get

$$\theta = \omega t - \phi \tag{14}$$

Where ϕ is the phase angle between e and r. From (13) equations (10) and (11) reduce to:

$$\begin{aligned} &\left(\frac{K}{m_d} - \omega^2\right) r = e\omega^2 \cos\phi \\ &\frac{c}{m_d}\omega r = e\omega^2 \sin\phi \end{aligned} \tag{15}$$

From last equations we have the following vectorial triangle:

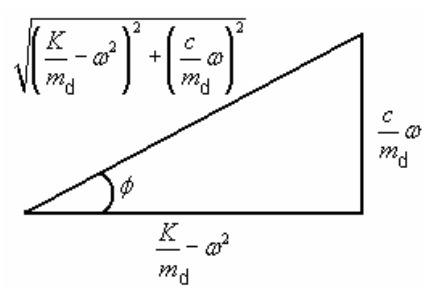

Figure 4. Vectorial triangle

The phase angle and the trigonometric expression of the first equation of (15) are obtained from the vectorial triangle as follows:

$$\tan\phi = \frac{\frac{c}{m_d}\omega}{\frac{K}{m_d} - \omega^2} \qquad \cos\phi = \frac{\frac{K}{m_d} - \omega^2}{\sqrt{\left(\frac{K}{m_d} - \omega^2\right)^2 + \left(\frac{c}{m_d}\omega\right)^2}} \tag{16}$$

Substituting the cosine term of (16) in the equation of motion in the radial direction, and solving for r we obtain the amplitude of motion for the SDOF system:

$$r = \frac{m_d e\omega^2}{\sqrt{\left(K - m_d\omega^2\right)^2 + (cm_d)^2}} \tag{17}$$

The wireless accelerometer mounted on the shaft allows modeling of the system in the rotating coordinate system because it is sensitive only in the radial direction $\vec{r}$, where the vibration parameters are involved due to the bending behavior of the shaft in that direction. This condition allows us to model the system in a fixed coordinate system relative to the accelerometer assuming the shaft fixed at the ends, and the rotation of the shaft is replaced by the harmonic force F(ωt) caused by the rotating unbalanced disk, which excites the system at the middle as shown before in Figure 3 (a).

This system can be represented with a free body diagram for a single degree of freedom system, where m_d is the mass of the disk and K is the stiffness of the shaft, which can be modeled as a spring as shown in Figure 5.

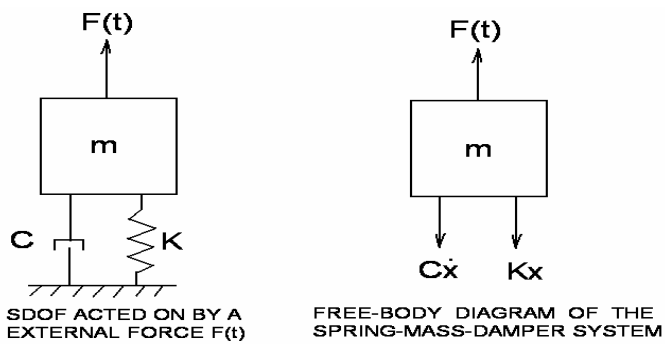

Figure 5. Free body diagram of a simplified SDOF system

The magnitude of the maximum deflection in the middle of the shaft shown in the Figure 6 can be obtained from the condition of equilibrium of the force P of the deflected shaft. This force is proportional to the deflection and can be represented as P=Kδ. The maximum deflection for a shaft fixed at both ends is well demonstrated at [11] Gere and Timoshenko.

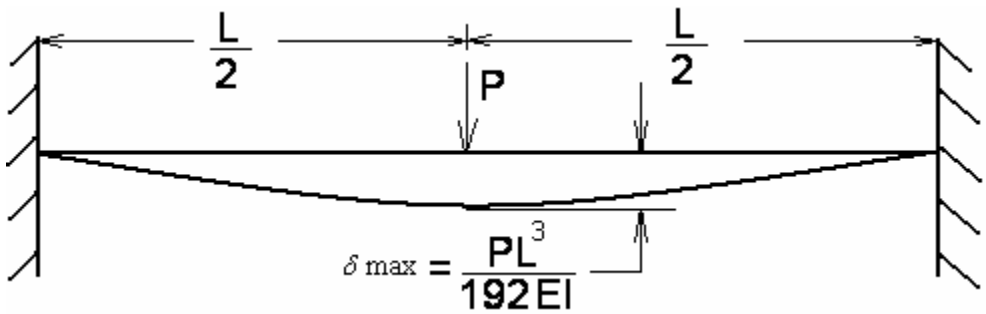

Figure 6. Maximum Deflection in the Middle of the Shaft

The stiffness of the shaft can be obtained from the last relation for a single degree of freedom system as

$$K = \frac{192EI}{L^3} \quad where \quad I = \frac{\pi r^4}{4} \tag{18}$$

The critical speed of the shaft is that speed at which the number of revolutions per second of the shaft is equal to the frequency of its first natural vibration is calculated taken the properties and geometry of the shaft from Table 1.

$$\omega_a = \sqrt{\frac{K}{m}} = 64.6608[rad/seg] \tag{19}$$

The critical speed is usually expressed in Hz :

$$\omega_c = \frac{1}{2\pi}\sqrt{\frac{192EI}{L^3 m}} = 10.2911[Hz] \tag{20}$$

3.2 Dynamic Analysis of the Uncracked Shaft in Forced Flexural Vibration

Once the harmonic force acting on the shaft due to the unbalance disk is derived for the rotating coordinate system in the radial direction, the vibration parameters and the flexural vibration of the shaft at any position and any time are derived employing the Euler – Bernoulli theory, which consider only lateral flexural deflections and that the plane cross section on a beam remains a plane during flexure. The generalized problem is considered as shown in the next figure:

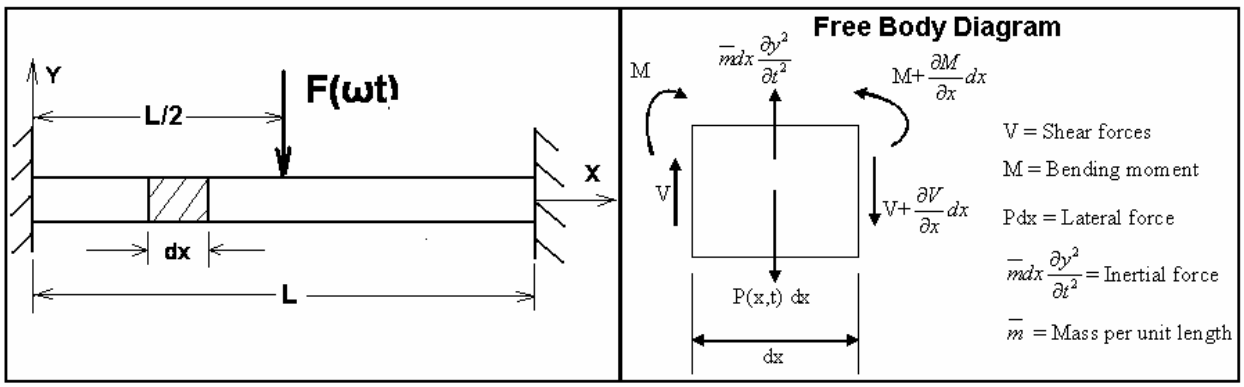

Figure 7. Shaft in forced vibration – Generalized case

The equation of motion perpendicular to the X axis of the deflected beam was obtained by equating to zero the sum of the forces in the free body diagram shown in Figure 7.

$$\frac{\partial V}{\partial x} + \bar{m}\frac{\partial^2 y}{\partial t^2} = P_{(x,t)} \tag{21}$$

From the bending theory, we have the relations:

$$V = \frac{\partial M}{\partial x} \qquad M = EI\frac{\partial^2 y}{\partial x^2} \qquad V = EI\frac{\partial^3 y}{\partial x^3} \tag{22}$$

Where, E = Young's Modulus of Elasticity and I = Moment of inertia of the cross section and were considered constant. Replacing (22) in (21):

$$EI\frac{\partial^4 y}{\partial x^4} + \bar{m}\frac{\partial^2 y}{\partial t^2} = P_{(x,t)} \tag{23}$$

It is seen that equation (23) is a partial differential equation of fourth order that describes the vibration of the rotating shaft in the rotating coordinate system. Only lateral flexural deflections were considered. The homogeneous differential equation was solved by separation of variables giving the modal deflection of the shaft at any position and time.

3.2.1 Solution of the Equation of Motion in Free Vibration

For free vibration (p(x,t) = 0) reduces to the homogeneous differential equation:

$$E\,I\,\frac{\partial^4 y}{\partial x^4} + \overline{m}\,\frac{\partial^2 y}{\partial t^2} = 0 \qquad \textbf{(24)}$$

Applying the method of separation of variables assuming a product solution

$$y(x,t) = \Phi(x)\,f(t) \qquad \textbf{(25)}$$

Substituting in (24) yields:

$$EI \cdot f(t)\frac{\partial^4 \Phi_{(x)}}{\partial x^4} + \overline{m} \cdot \Phi_{(x)}\frac{\partial^2 f_{(t)}}{\partial x^2} = \omega_n^2 \qquad \textbf{(26)}$$

$$ODE\ 1: \qquad \frac{d^2 f_{(t)}}{dx^2} = -\omega_n^2 f \qquad \textbf{(27)}$$

The characteristic equation is:

$$r^2 + \omega_n^2 = 0 \quad \rightarrow \quad r_{1,2} = \pm i\omega_n \qquad \textbf{(28)}$$

The solution is:

$$f(t) = C_1 \cos(\omega_n t) + C_2 \sin(\omega_n t) \qquad \textbf{(29)}$$

$$ODE\ 2: \qquad \frac{d^4 \Phi_{(x)}}{dx^4} = \omega_n^2 \cdot \frac{\overline{m}}{EI}\Phi_{(x)} = \omega_n^2 c^2 \Phi_{(x)}, \qquad c = \sqrt{\frac{\overline{m}}{EI}} \qquad \textbf{(30)}$$

The characteristic equation is:

$$r^4 - \omega_n^2 c^2 = 0 \quad \rightarrow \quad (r^2 + \omega_n c)(r^2 - \omega_n c)$$
$$\therefore \qquad r_{1,2} = \pm i\sqrt{\omega_n c} \qquad\qquad r_{3,4} = \pm\sqrt{\omega_n c} \tag{31}$$

The solution of this equation is:

$$\Phi_{(x)} = C_3 \cos(\sqrt{\omega_n c}x) + C_4 \sin(\sqrt{\omega_n c}x) + C_5 \cosh(\sqrt{\omega_n c}x) + C_6 \sinh(\sqrt{\omega_n c}x) \tag{32}$$

$$\Phi''_{(x)} = -C_3\omega_n c\cos(\sqrt{\omega_n c}x) + C_4\omega_n c\sin(\sqrt{\omega_n c}x) + C_5\omega_n c\cosh(\sqrt{\omega_n c}x) + C_6\omega_n c\sinh(\sqrt{\omega_n c}x) \tag{33}$$

3.2.2 Eigen Value Problem for the Shaft with Both Ends Fixed

The boundary conditions at X=0 for the shaft with both ends fixed are:

$$Y_{(0,t)} = 0 \qquad\qquad \Phi_{(0)} = 0,$$
$$Y'_{(0,t)} = 0 \qquad\qquad \Phi'_{(0)} = 0 \tag{34}$$

Applying the boundary conditions into equations (32) and (33) gives:

$$\Phi_{(0)} = C_3 + C_5 = 0 \Rightarrow C_5 = -C_3 \tag{35}$$

$$\Phi_{(x)} = C_3[\cos(\sqrt{\omega_n c}x) - \cosh(\sqrt{\omega_n c}x)] + C_4 \sin(\sqrt{\omega_n c}x) + C_6 \sinh(\sqrt{\omega_n c}x)$$

$$\Phi'_{(x)} = \sqrt{\omega_n c}\left\{C_3[-\sin(\sqrt{\omega_n c}x) - \sinh(\sqrt{\omega_n c}x)] + C_4 \cos(\sqrt{\omega_n c}x) + C_6 \cosh(\sqrt{\omega_n c}x)\right\}$$

$$\Phi_{(0)} = C_4 + C_6 = 0 \Rightarrow C_6 = -C_4 \tag{36}$$

$$\Phi_{(x)} = C_3[\cos(\sqrt{\omega_n c}x) - \cosh(\sqrt{\omega_n c}x)] + C_4[\sin(\sqrt{\omega_n c}x) - \sinh(\sqrt{\omega_n c}x)] \tag{37}$$

$$\Phi'_{(x)} = \sqrt{\omega_n c}\left\{C_3[-\sin(\sqrt{\omega_n c}x) - \sinh(\sqrt{\omega_n c}x)] + C_4[\cos(\sqrt{\omega_n c}x) - \cosh(\sqrt{\omega_n c}x)]\right\}$$

At X=L $\quad Y_{(L,t)} = 0 \qquad\qquad \Phi_{(L)} = 0,$

$$Y'_{(L,t)} = 0 \qquad\qquad \Phi'_{(L)} = 0 \tag{38}$$

Applying the boundary conditions into equations (32) and (33) gives:

$$\Phi_{(L)} = C_3[\cos(\sqrt{\omega_n c}L) - \cosh(\sqrt{\omega_n c}L)] + C_4[\sin(\sqrt{\omega_n c}L) - \sinh(\sqrt{\omega_n c}L)] = 0 \tag{39}$$

$$\Phi'_{(L)} = C_3[-\sin(\sqrt{\omega_n c}L) - \sinh(\sqrt{\omega_n c}L)] + C_4[\cos(\sqrt{\omega_n c}L) - \cosh(\sqrt{\omega_n c}L)] = 0 \tag{40}$$

Equating the determinant of the system above we have:

$$0 = \cos^2(\sqrt{\omega_n c}L) - \cos(\sqrt{\omega_n c}L)\cosh(\sqrt{\omega_n c}L) - \cosh(\sqrt{\omega_n c}L)\cos(\sqrt{\omega_n c}L) + \cosh^2(\sqrt{\omega_n c}L)$$
$$-[-\sin^2(\sqrt{\omega_n c}L) + \sin(\sqrt{\omega_n c}L)\sinh(\sqrt{\omega_n c}L) - \sinh(\sqrt{\omega_n c}L)\sin(\sqrt{\omega_n c}L) + \sinh^2(\sqrt{\omega_n c}L)] \quad \textbf{(41)}$$

$$0 = 1 - 2\cos(\sqrt{\omega_n c}L)\cosh(\sqrt{\omega_n c}L) + \cosh^2(\sqrt{\omega_n c}L) - \sinh^2(\sqrt{\omega_n c}L)$$
$$As \quad \cosh^2(\sqrt{\omega_n c}L) - \sinh^2(\sqrt{\omega_n c}L) = 1, then \quad \textbf{(42)}$$

$$-2\cos(\sqrt{\omega_n c}L)\cosh(\sqrt{\omega_n c}L) + 2 = 0 \quad \textbf{(43)}$$

$$\therefore \ \cos(\sqrt{\omega_n c}L)\cosh(\sqrt{\omega_n c}L) - 1 = 0 \quad \textbf{(44)}$$

3.2.3 Eigen Values Estimation

Equation (43) is a transcendental equation for the positive eigenvalues $\sqrt{\omega_n c}L$. The eigen values must satisfy last expression in the intercepts of the curves given by the next functions:

$$Z = \frac{1}{\cosh(\sqrt{\omega_n c}L)} \quad and \quad Z = \cos(\sqrt{\omega_n c}L) \quad \textbf{(45)}$$

The values of the intercepts are used to calculate a relation for the eigen values and the natural frequencies as shown in the next figure:

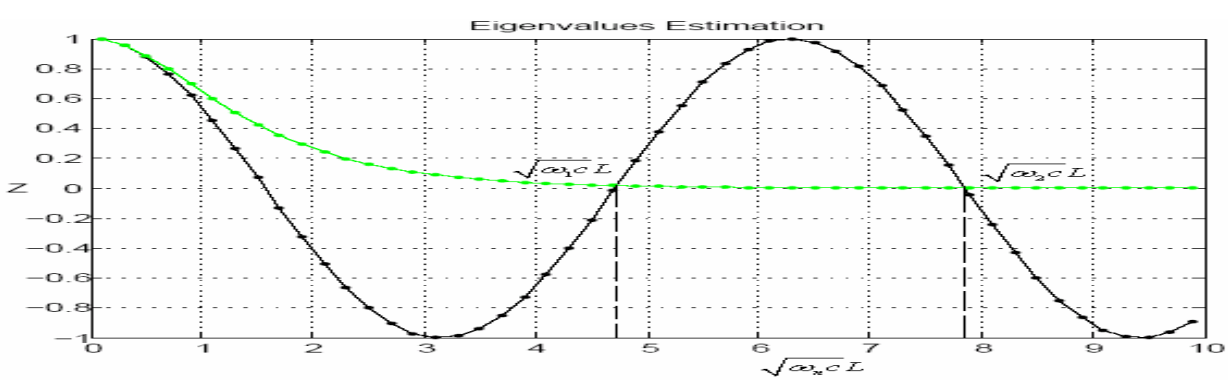

Figure 8. Eigen values estimated graphically

Finding a relation for the eigen values that intersect both curves gives the following expression for the natural frequencies:

$$\omega_n = \left(\frac{(2n+1)\pi}{2L} \right)^2 \sqrt{\frac{EI}{\bar{m}}} \tag{46}$$

3.2.4 Mode Shapes of the Shaft with Fixed Ends

From equation (39) , it follows that

$$C_3 = \frac{(\cos\sqrt{\omega_n c}L - \cosh\sqrt{\omega_n c}L) - 1}{\sin\sqrt{\omega_n c}L - \sinh\sqrt{\omega_n c}L} C_4 \tag{47}$$

C4 is arbitrary and can be assumed as 1. To each value of natural frequency obtained in (46) there corresponds a normal mode

$$\Phi_n(x) = \cosh(\sqrt{\omega_n c}x) - \cos(\sqrt{\omega_n c}x) - \sigma_n(\sinh(\sqrt{\omega_n c}x) - \sin(\sqrt{\omega_n c}x)) \tag{48}$$

Where:

$$\sigma_n = \frac{\cosh(\sqrt{\omega_n c}L) - \cos(\sqrt{\omega_n c}L)}{\sinh(\sqrt{\omega_n c}L) - \sin(\sqrt{\omega_n c}L)} \tag{49}$$

The following figures show the first three mode shapes for the shaft with the both ends fixed in the rotating coordinate system relative to the accelerometer:

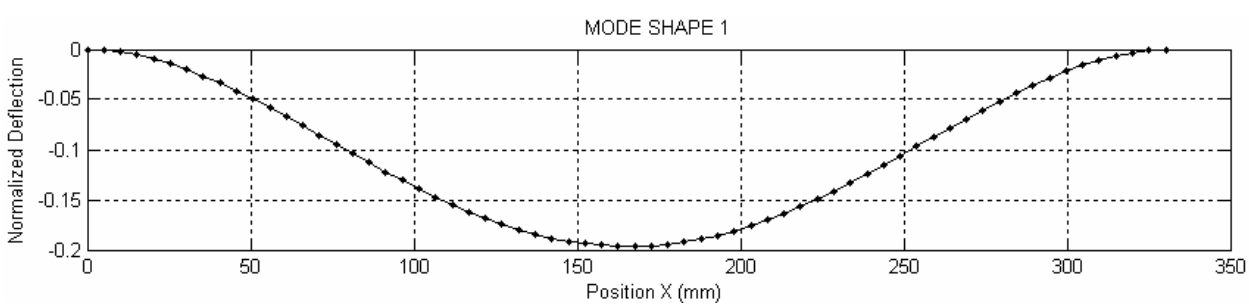

Figure 9. First mode shape of the uncracked shaft

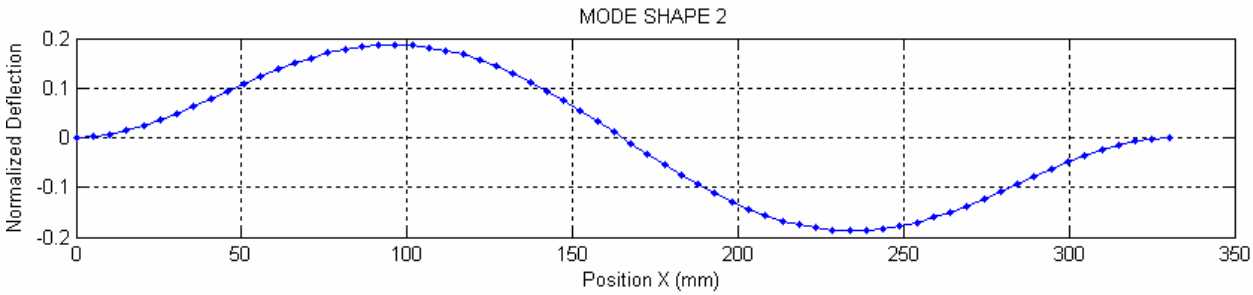

Figure 10. Second mode shape of the uncracked shaft

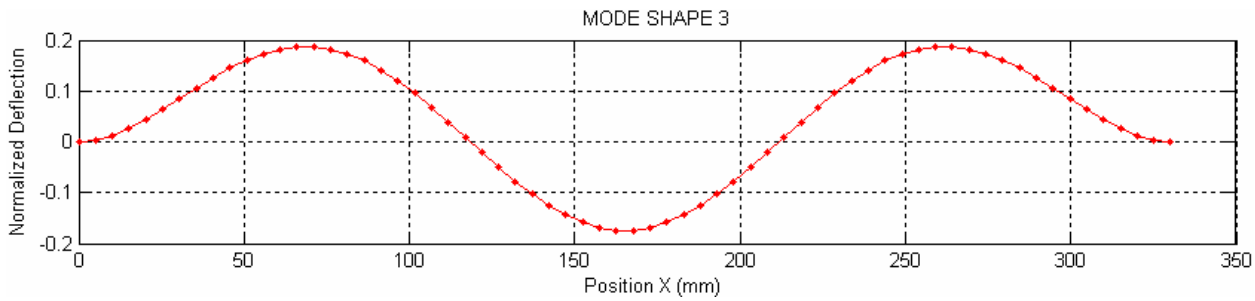

Figure 11. Third mode shape of the uncracked shaft

3.2.5 Shaft under Forced Vibration

Once the homogeneous problem is solved, the modal function $\Phi_{(x)}$ is used to solve the forced vibration problem of the beam subjected to a harmonic force $P_{(x,t)}$.

$$P_{(t)} = m_d e\omega^2 \cos(\omega t - \theta) = P_0 \cos(\omega t - \theta) \quad where \quad P_0 = m_d e\omega^2 \tag{50}$$

The partial differential equation becomes:

$$EI\frac{\partial^4 y}{\partial x^4} + \overline{m}\frac{\partial^2 y}{\partial t^2} = P_0 \cos(\omega t - \theta) \qquad P_0 = m_d e\omega^2 \tag{51}$$

m_d is the mass of the disk mounted on the rotating shaft, e is the eccentricity and ω is the driving frequency.

Assuming that the general solution of this equation may be expressed by the summation of the products of normal modes $\Phi_{(x)}$ multiplied by the factors $Z_{n(t)}$ which are to be determined. Hence we have the product solutions:

$$Y_{(x,t)} = \sum_{n=1}^{\infty} \Phi_{n(x)} Z_{n(t)} \tag{52}$$

Where the normal modes $\Phi_{n(x)}$ satisfy the differential equation (30) rewritten down:

$$\frac{\partial^4 \Phi_{n(x)}}{\partial x^4} = \omega_n^2 \cdot \frac{\overline{m}}{EI} \Phi_{n(x)} = \omega_n^2 c^2 \Phi_{n(x)}, \qquad c = \sqrt{\frac{\overline{m}}{EI}} \tag{53}$$

The normal modes should also satisfy the specific force boundary conditions at the ends of the shaft. Substitution of (52) in (51) gives:

$$EI \sum_n \Phi_{n(x)}^{IV} Z_{n(t)} = P_{(x,t)} - \overline{m} \sum_n \Phi_{n(x)} \ddot{Z}_{n(t)} \tag{54}$$

From (53) we have:

$$EI \frac{\partial^4 \Phi_{n(x)}}{\partial x^4} = \omega_n^2 \cdot \overline{m} \cdot \Phi_{n(x)} \tag{55}$$

Multiplying both sides by $\Phi_{m(x)} dx$ and integrating between 0 and L results in

$$\omega_m^2 Z_{m(t)} \int_0^L \overline{m} \Phi_{m(x)}^2 dx = \int_0^L \Phi_{m(x)} P_{(x,t)} dx - \ddot{Z}_{n(t)} \cdot \int_0^L \overline{m} \Phi_{m(x)}^2 dx \tag{56}$$

All terms which contain products of different indices ($n \neq m$) vanish from the summation in (56) due to the orthogonality conditions between normal modes. Equation (56) can be written as:

$$M_n \ddot{Z}_{n(t)} + \omega_n^2 M_n Z_{n(t)} = F_{n(t)}, \qquad n=1,2,3... \tag{57}$$

Where:

$$M_n = \int_0^L \overline{m}\,\Phi^2_{m(x)}dx \qquad and \qquad F_{n(t)} = \int_0^L \Phi_{m(x=L/2)} P_{(\omega,t)} dx \tag{58}$$

M_n is the modal mass and $F_{n(t)}$ the modal force. Last equation is analogous to the modal equation for discrete systems. Modal damping could certainly be introduced by simply adding the damping term in equation (57) as follows:

$$M_n \ddot{Z}_{n(t)} + C_n \dot{Z}_{n(t)} + \omega_n^2 M_n Z_{n(t)} = F_{n(t),} \qquad n=1,2,3... \tag{59}$$

Or

$$\ddot{Z}_{n(t)} + 2\xi_n \omega_n \dot{Z}_{n(t)} + \omega_n^2 Z_{n(t)} = \frac{F_{n(t)}}{M_n} \qquad n = 1, 2, 3... \tag{60}$$

Where $\xi_n = \dfrac{C_n}{C_{ncr}}$ is the modal damping and $K = M_n \omega_n^2$ the modal stiffness.

Replacing $P_{(\omega,t)}$ from equation (51) into the modal force term of equation (60) then the modal force term becomes:

$$\frac{F_{n(t)}}{M_n} = I_n P_0 \cos(\omega t + \theta) dx, \quad where: \quad I_n = \frac{\int_0^L \Phi_{n(x=L/2)} dx}{\int_0^L \overline{m}\,\Phi^2_{n(x)} dx} \tag{61}$$

Neglecting damping, the equation (61) becomes:

$$\ddot{Z}_{n(t)} + \omega_n^2 Z_{n(t)} = I_n P_0 \cos(\omega t - \theta) \tag{62}$$

The last equation is solved using the method of the undetermined coefficients for the initial conditions:

$$Z_{(0)} = f(x) \qquad \frac{dZ}{dt}_{(0)} = 0 \tag{63}$$

The characteristic equation of the homogeneous differential equation is:

$$r^2 + \omega_n^2 = 0 \qquad r = \pm i\omega_n \tag{64}$$

The solution of the homogeneous problem gives us the complementary function:

$$Z_{c(t)} = C_7 \cos(\omega_n t) + C_8 \sin(\omega_n t) \tag{65}$$

In order to get a particular solution we assume a solution:

$$Z_{p(t)} = A\cos(\omega t - \theta) + B\sin(\omega t - \theta) \tag{66}$$

$$\begin{aligned} \dot{Z}_{p(t)} &= -A\omega \sin(\omega t - \theta) + B\omega \cos(\omega t - \theta) \\ \ddot{Z}_{p(t)} &= -A\omega^2 \cos(\omega t - \theta) - B\omega^2 \sin(\omega t - \theta) \end{aligned} \tag{67}$$

Replacing last terms in the differential equation we have:

$$\begin{aligned} \ddot{Z}_{n(t)} + \omega_n^2 Z_{n(t)} &= -A\cos(\omega t - \theta) - B\sin(\omega t - \theta) + \omega_n{}^2 [A\cos(\omega t - \theta) - B\sin(\omega t - \theta)] \\ &= I_n P_0 \cos(\omega t - \theta) \end{aligned} \tag{68}$$

Equating coefficients we have:

$$B = 0 \quad and \quad -A\omega^2 + \omega_n^2 A = P_0 I_n \quad \rightarrow A = \frac{P_0 I_n}{(\omega_n^2 - \omega^2)} \tag{69}$$

Then, the particular solution is: $$Z_{p(t)} = \frac{P_0 I_n}{(\omega_n^2 - \omega^2)} \cos(\omega t - \theta) \tag{70}$$

The general solution is the sum of the complementary and the particular solution, then:

$$Z_{n(t)} = C_7 \cos(\omega_n t) + C_8 \sin(\omega_n t) + \frac{P_0 I_n}{(\omega_n^2 - \omega^2)} \cos(\omega t - \theta) \tag{71}$$

Applying the initial conditions we have:

$$Z_{(0)} = f(x) \quad \rightarrow \quad C_7 = f(x) + \frac{P_0 I_n}{(\omega_n^2 - \omega^2)}\cos(\theta)$$

$$\therefore \quad Z_{n(t)} = [f(x) + \frac{P_0 I_n}{(\omega_n^2 - \omega^2)}\cos(\theta)]\cos(\omega_n t) + C_8 \sin(\omega_n t) + \frac{P_0 I_n}{(\omega_n^2 - \omega^2)}\cos(\omega t - \theta) \tag{72}$$

$$\dot{Z}_{(0)} = 0 \qquad \rightarrow C_8 = 0$$

$$\therefore \quad Z_{n(t)} = f(x)\cos(\omega_n t) + C_8 \sin(\omega_n t) + \frac{P_0 I_n}{(\omega_n^2 - \omega^2)}[\cos(\omega_n t) - \cos(\omega t - \theta)] \tag{73}$$

$$\therefore \quad Z_{n(t)} = f(x)\cos(\omega_n t) + \frac{P_0 I_n}{(\omega_n^2 - \omega^2)}[\cos\theta \cdot \cos(\omega_n t) + \cos(\omega t - \theta)] \tag{74}$$

The modal deflection at any section of the shaft at any time is given by the product solution:

$$y_{n(x,t)} = \phi_{n(x)} Z_{n(t)} \tag{75}$$

In which $\phi_{n(x)}$ is the modal shape defined for a fixed shaft by equation (4.43) and $Z_{n(t)}$ is the modal response. Substitution of both equations becomes:

$$y_{n(x,t)} = \sum_{n=1}^{\infty} \phi_{n(x)} \{ f(x)\cos(\omega_n t) + \frac{P_0 I_n}{(\omega_n^2 - \omega^2)}[\cos\theta \cdot \cos(\omega_n t) + \cos(\omega t - \theta)]\} \tag{76}$$

where, $\Phi_n(x) = \cosh(\sqrt{\omega_n c}x) - \cos(\sqrt{\omega_n c}x) - \sigma_n(\sinh(\sqrt{\omega_n c}x) - \sin(\sqrt{\omega_n c}x))$

$$f(x) = -\frac{P_0 L^3}{192EI} \qquad I_n = \frac{\int_0^L \Phi_{n(x)} dx}{\int_0^L \bar{m}\Phi_{n(x)}^2 dx} \qquad P_0 = m_d e\omega^2 \qquad \omega_n = \left(\frac{(2n+1)\pi}{2L}\right)^2 \sqrt{\frac{EI}{\bar{m}}}$$

$$\sigma_n = \frac{\cos(\sqrt{\omega_n c}L) - \cosh(\sqrt{\omega_n c}L)}{\sin(\sqrt{\omega_n c}L) - \sinh(\sqrt{\omega_n c}L)} \qquad \int_0^L \bar{m}\Phi_{n(x)}^2 dx = \frac{\bar{m}L}{2}$$

The solution of the non-homogeneous partial differential modal equation derived constitutes the displacement of any point of the shaft at any time at certain driving frequency.

Solution of the equation at three different times is shown in the Figure 12 for a driving frequency of 4 Hz and taking the properties of the shaft and disk indicated in Table 1.

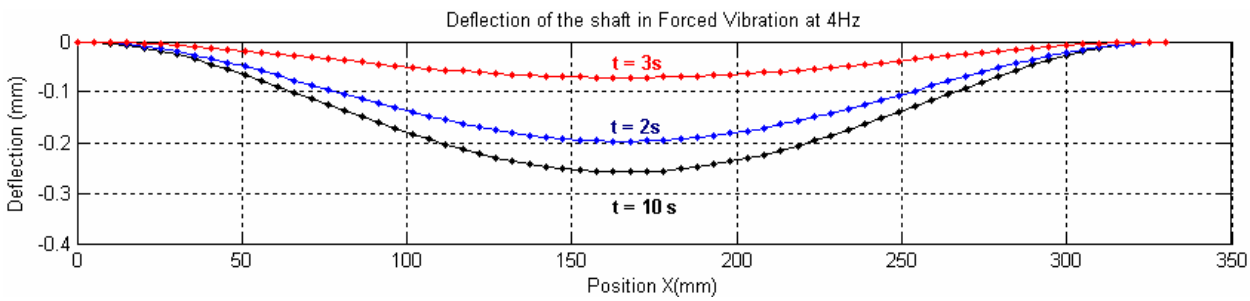

Figure 12. Deflection of the shaft at different times

The acceleration expression is given by the second derivative in the time for the equation (76) as:

$$\ddot{Y}_{n(x,t)} = \sum_{n=1}^{\infty} \phi_{n(x)} \{ -f(x)\omega_n^2 \cos(\omega_n t) - \frac{P_0 I_n \omega_n^2}{(\omega_n^2 - \omega^2)} [\cos\theta \cdot \cos(\omega_n t) + \cos(\omega t - \theta)] \} \quad \textbf{(77)}$$

3.3 Random Signal Analysis

The accelerometer used to measure the acceleration signal of the system contains noise, which introduces random components that make it difficult to measure data in a deterministic fashion. The value τ is the time difference between the values at which the signal x(t) is sampled. The autocorrelation function of a stationary sample function denoted as $R_{xx}(\tau)$ is the expect value of the product $x(t)x(t+\tau)$ computed along the time axis, this is interpreted as the average of this product for many record data. The prefix auto refers to the fact that term $x(t)x(t+\tau)$ is the terms of the values of the same sample at two different times.

$$R_{xx}(\tau) = E[x(t) \bullet x(t+\tau)] \quad or \quad R_{xx}(\tau) = \lim_{\tau \to \infty} \frac{1}{T} \int_0^T x(t)x(t+\tau)dt \quad \textbf{(78)}$$

Acceleration signal at the nodes of the shaft were brought to the frequency domain using the power spectral density function, which provides the frequency description of the harmonic acceleration signal. Noise is reduced when the signal is averaged with the autocorrelation function in order to obtain a parameter that represents better the stationary random (noisy) signal.

The Fourier transform of a function x(t) is denoted by X(ω) and is defined by

$$X(\omega) = \int_{-\infty}^{\infty} x(t) e^{-j\omega t} dt \tag{79}$$

Last expression transforms the variable x(t) from a function of time into a function of frequency ω. The inversion of this transform is performed by

$$x(t) = \frac{1}{2\pi} \int_{-\infty}^{\infty} X(\omega) e^{j\omega t} d\omega \tag{80}$$

The Fourier transform of the autocorrelation function Rxx(τ) defines the power spectra density (PSD) denoted by

$$S_{xx}(\omega) = \frac{1}{2\pi} \int_{-\infty}^{\infty} R_{xx}(\tau) e^{-j\omega t} d\tau \tag{81}$$

Power Spectral Density Amplitudes (PSDA) of the shaft provide the frequency description of the noisy acceleration signal, therefore they were taken as the vibration parameter at three different positions of the shaft.

Next figure corresponds to the Power Spectral Density Amplitudes of Acceleration (PSDAA) at different positions of the shaft estimated applying the PSD to the simulated signal described by the equation (77) introducing the properties indicated in Table 1 and vibrating at a driving frequency of 4 Hz.

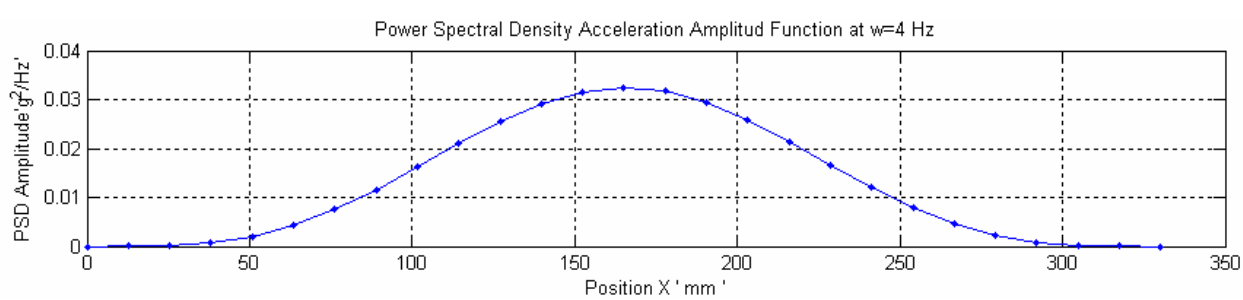

Figure 13. PSD Acceleration Amplitudes at different position of the shaft rotating at 4 Hz

3.4 Conclusions

The harmonic excitation force of the unbalanced disk was derived from a vectorial analysis based on two degrees of freedom system and then reduced to one degree of freedom in the direction of sensitivity of the accelerometer.

A partial differential equation of the loaded vibration shaft in the rotating coordinate was derived from the theory of mechanics of materials based on the Euler Bernoulli theory for the uncracked shaft considered fixed in both ends relative to the accelerometer.

The solution of the homogeneous problem was obtained by means of separation of variables method to solve the eigen value problem, whereby vibration parameter expressions such as: natural frequencies, mode shape functions, deflections, and accelerations were derived. The modal function solution obtained by this method was employed within the undetermined coefficient method to solve the non-homogeneous problem due to the harmonic force induced by the unbalance disk in the middle of the shaft.

For a given driving frequency, the Power Spectral Density Amplitudes of Acceleration (PSDAA) obtained at different points of the shaft resulted to be function of the mode shapes and constitute a vibration characteristic of the continuous shaft as shown in Figure 13.

From equation (46) the first three natural frequencies of the shaft were estimated: 5.8295 Hz, 16.1932 Hz and 31.7386 Hz.

These results gave the insight to model the cracked shaft employing the finite element method to obtain the amplitudes of acceleration signals at the boundaries of discretized elements of the shaft including the crack element aimed to obtain the sensitivity vibration parameters to be associated with the crack positions and depths.

4 Finite Element Model of the Rotating Cracked Shaft

Finite Element Method was employed to model the cracked and uncracked shaft rotating with the unbalance disk acting on the shaft as a constant harmonic force in order to verify theoretically the sensitivity and uniqueness of the acceleration response in the frequency domain for different crack positions and depths. A code was built employing the software MATLAB 7.1 for the data estimation. These parameters were used to solve the inverse problem; knowing the frequency response amplitude of acceleration at three different points of the shaft, find the crack characteristics by means of Neural Networks.

The crack propagation is a slow process, it takes several cycles of rotation for the crack to advance a small distance over microns, therefore the shaft was considered with a transverse open crack of 0.8 mm width for the purpose of the dynamic analysis as shown in the Figure 14.

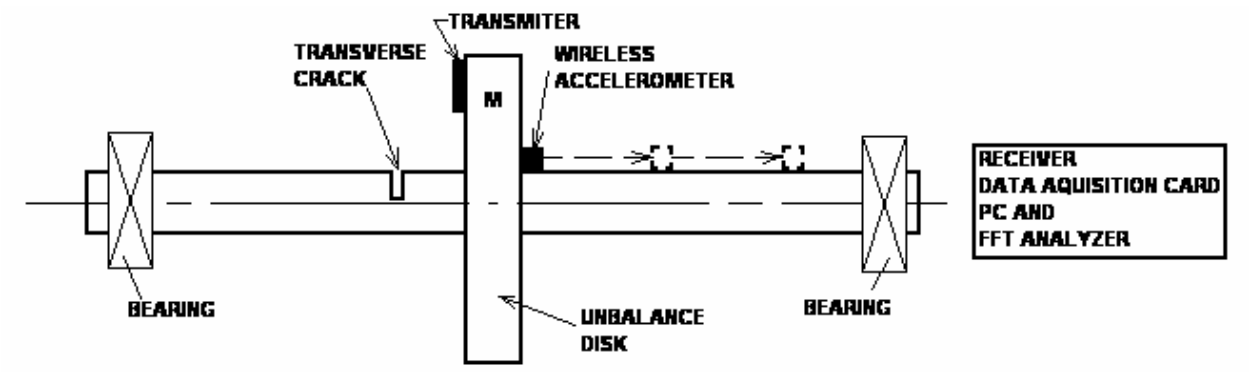

Figure 14. Cracked Shaft Model

The open crack was considered as a small element with reduced stiffness within the finite element model. Only one crack is assumed for this study, and external damping was neglected. Wireless sensor directly mounted on the shaft allow to analyze the rotating system in a static frame relative to the sensor, therefore the model is assumed as a fixed beam carrying the disk and experiencing mainly flexural stresses due to the harmonic excitation of the disk at the midspan.

4.1 Derivation of the Element Stiffness Matrix

The model used to simulate the rotor system was constructed using the Euler-Beam Finite Element Analysis. Each element's mode shape was approximated using a cubic equation, in order to ensure the continuity of the deflection and the slope at the nodes of the model.

Figure 15 illustrates a uniform beam segment with distributed inertial and stiffness properties, the displacements and rotations are identified and the beam's mass is assumed uniformly distributed throughout its length.

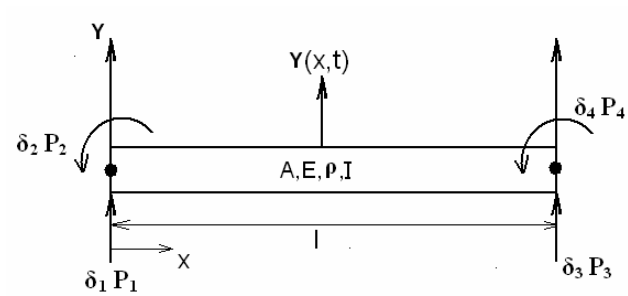

Figure 15. Euler Bernoulli Beam Finite Element

The stiffness matrix for a beam segment is obtained by establishing the relation between static forces and moments designated as P1, P2, P3 and P4 with the corresponding linear and angular displacements δ1, δ2, δ3 and δ4 at the end of the beam segment as indicated in the last figure. These parameters are called the nodal coordinates. The differential equation for small transverse displacement of a beam is given by:

$$EI\frac{d^2y}{dx^2} = M(x) \qquad \textbf{(82)}$$

Where M(x) is the bending moment and y is the transverse displacement. This equation is equivalent to:

$$EI\frac{d^4y}{dx^4} = P(x) \qquad \textbf{(83)}$$

$$\textit{Since} \qquad \frac{dM(x)}{dx} = V(x) \qquad \frac{dV(x)}{dx} = P(x) \qquad \textbf{(84)}$$

Where P(x) is the beam load per unit length and V(x) is the shear force.

The stiffness coefficient kij is defined as the force at nodal coordinate i due to a unit displacement at nodal coordinate j while all other nodal coordinates are maintained at zero displacement. In order to find the expressions of the stiffness coefficients the static deflection curves due to a unit displacement at nodal coordinate should be found considering the element free of loads P(x)=0, except for the forces in the nodes P1, P2, P3 and P4. In this case equation (83) is reduced to:

$$\frac{d^4 y}{dx^4} = 0 \qquad \textbf{(85)}$$

Successive integrations of equation (85) yields

$$\frac{d^3 y}{dx^3} = C_1, \quad \frac{d^2 y}{dx^2} = C_1 x + C_2, \quad \frac{dy}{dx} = \frac{1}{2} C_1 x^2 + C_2 x + C_3, \quad y = \frac{1}{6} C_1 x^3 + \frac{1}{2} C_2 x^2 + C_3 x + C_4 \qquad \textbf{(86)}$$

The constants of integration are calculated using the boundary conditions for each static deflection curve resulting in an algebraic system of four equations to determine the constants C1, C2, C3 and C4.

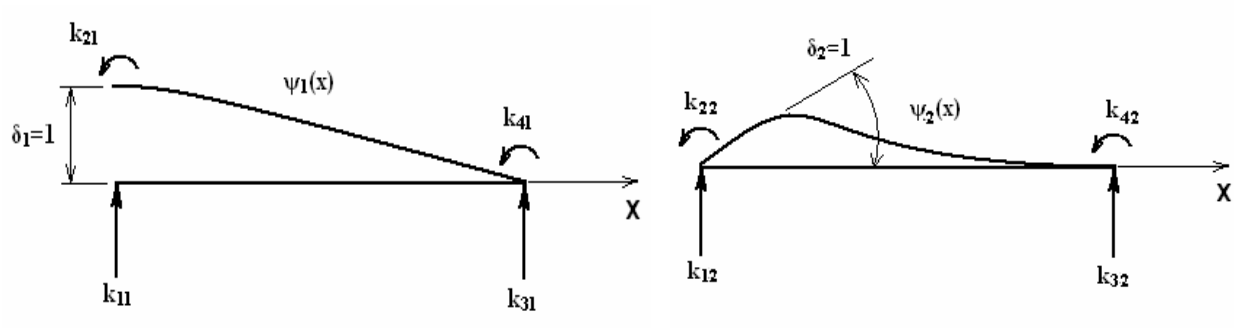

Figure 16. Static deflection curves due to unit displacement at nodal coordinate 1

The boundary conditions to obtain the function ψ1(x) shown in Figure 16 (a) are as follows:

$$at\ x = 0 \qquad y(0) = 1 \quad and \quad \frac{dy(0)}{dx} = 0 \qquad \textbf{(87)}$$

$$at\ x = L \qquad y(L) = 0 \quad and \quad \frac{dy(L)}{dx} = 0 \tag{88}$$

Substituting last boundary conditions in the equation (86) and solving the algebraic system we get the deflected curve equation of the beam segment shown in the Figure 16 (a).

$$\psi_1(x) = 1 - 3\left(\frac{x}{L}\right)^2 - 2\left(\frac{x}{L}\right)^3 \tag{89}$$

Proceeding in the same manner, we obtain the equations of the deflected curves for the other cases.

$$\psi_2(x) = x\left(1 - \frac{x}{L}\right)^2, \quad \psi_3(x) = 3\left(\frac{x}{L}\right)^2 - 2\left(\frac{x}{L}\right)^3, \quad \psi_4(x) = \frac{x^2}{L}\left(\frac{x}{L} - 1\right) \tag{90}$$

These functions are called the Hermitian shape functions and the displacement resulting from an arbitrary nodal displacement δi=1 is ψi(x) δi. Thus the total deflection y(x) due to arbitrary displacements at the nodal coordinates of the beam is obtained by superposition as

$$y(x) = \psi_1(x)\delta_1 + \psi_2(x)\delta_2 + \psi_3(x)\delta_3 + \psi_4(x)\delta_4 \tag{91}$$

Applying the principle of virtual work, which states that for an elastic system in equilibrium, the work done by the external forces is equal to the work of internal forces during the virtual displacement. The external work W_E is equal to the product of the force kij displaced by δ1=1, that is

$$W_E = k_{12}\delta_1 \tag{92}$$

Considering the work performed by the bending moment, we obtain for the internal work

$$W_I = \int_0^L M(x)d\theta \tag{93}$$

The transverse deflection of the beam is given by the equation (89), which is related to the bending moment through the differential equation. Substituting the second derivative we get

$$EI\psi_2''(x) = M(x) \tag{94}$$

The angular deflection dθ produced during the virtual displacement is related to the resulting transverse deflection of the beam ψ1(x) by

$$\frac{d\theta}{dx} = \frac{d^2\psi_1(x)}{dx^2} = \psi_1''(x) \quad \Rightarrow \quad d\theta = \psi_1''(x)dx \tag{95}$$

Equating the external virtual work WE with the internal virtual work W_I from above equations give the stiffness coefficient as

$$k_{12} = \int_0^L EI\psi_1''(x)\psi_2''(x)dx \tag{96}$$

Taking the derivative twice for the expressions ψ1 and ψ2 and replacing them in the last equation we get

$$k_{12} = EI\int_0^L \left(\frac{-6}{L^2} + \frac{12x}{L^3}\right)\left(\frac{-4}{L} + \frac{6x}{L^2}\right) \quad \Rightarrow \quad k_{12} = \frac{6EI}{L^2} \tag{97}$$

In general, any stiffness coefficient associated with the beam flexure can be expressed as

$$k_{ij} = \int_0^L EI\psi_i''(x)\psi_j''(x)dx \tag{98}$$

Evaluating all the coefficients of the stiffness matrix will result in the relation between the forces {P} and the displacement vector {δ} at the nodal coordinates with the beam element stiffness matrix [k] as shown

$$\begin{Bmatrix} P_1 \\ P_2 \\ P_3 \\ P_4 \end{Bmatrix} = \frac{EI}{L^3}\begin{bmatrix} 12 & 6L & -12 & 6L \\ 6L & 4L^2 & -6L & 2L^2 \\ -12 & -6L & 12 & -6L \\ 6L & 2L^2 & -6L & 4L^2 \end{bmatrix}\begin{Bmatrix} \delta_1 \\ \delta_2 \\ \delta_3 \\ \delta_4 \end{Bmatrix} \quad or \quad \{P\} = [k]\{\delta\} \tag{99}$$

4.2 Derivation of the Consistent Element Mass Matrix

The mass coefficients m_{ij} corresponding to the nodal coordinates of a beam element are defined as the force at the nodal coordinate i due to unit acceleration at nodal coordinate j while the other coordinates remain at zero acceleration. They are derived in the same fashion as the element stiffness coefficients. In the consistent mass method, it is assumed that the deflections resulting from unit dynamic displacements at the nodal coordinates of the beam element are given by the same shape functions $\psi_{1(x)}$, $\psi_2(x)$, $\psi_3(x)$ and $\psi_4(x)$. Equating the external and internal virtual work results in the elemental mass coefficient expression

$$m_{ij} = \int_0^L m(x)\psi_i\psi_j dx \qquad \textbf{(100)}$$

Calculating each beam mass coefficient using the last equation gives the following relation between inertial forces and acceleration at nodal coordinates

$$\begin{Bmatrix} P_1 \\ P_2 \\ P_3 \\ P_4 \end{Bmatrix} = \frac{mL}{420}\begin{bmatrix} 156 & 22L & 54 & -13L \\ 22L & 4L^2 & 13L & -3L^2 \\ 54 & 13L & 156 & -22L \\ -13L & -3L^2 & -22L & 4L^2 \end{bmatrix}\begin{Bmatrix} \ddot{\delta}_1 \\ \ddot{\delta}_2 \\ \ddot{\delta}_3 \\ \ddot{\delta}_4 \end{Bmatrix} \qquad \textbf{(101)}$$

4.3 Reduction of Dynamic Global Matrices

The system is discretized into six numbered elements represented in circles, degrees of freedom are shown with arrows and the connectivity nodes with points as shown in Figure 17. The dynamic condensation method proposed by Paz (1984) [20] as an extension of the Static Condensation Method is applied. Fixed degrees of freedom are reduced by expressing them in terms of the independent or primary degrees of freedom, the secondary degrees of freedom {Ys} (slopes 1-5) are condensed, and the primary degrees of freedom {Yp} are retained (deflections 6-10). The secondary degrees of freedom are arranged at the first s coordinates and the primary degrees of freedom are the last p coordinates. Thus the degrees of freedom are numbered leaving

the fixed nodal coordinates at last. In this case four of the nodal coordinates named as eleven are constrained and we have ten free coordinates corresponding to slope and displacement.

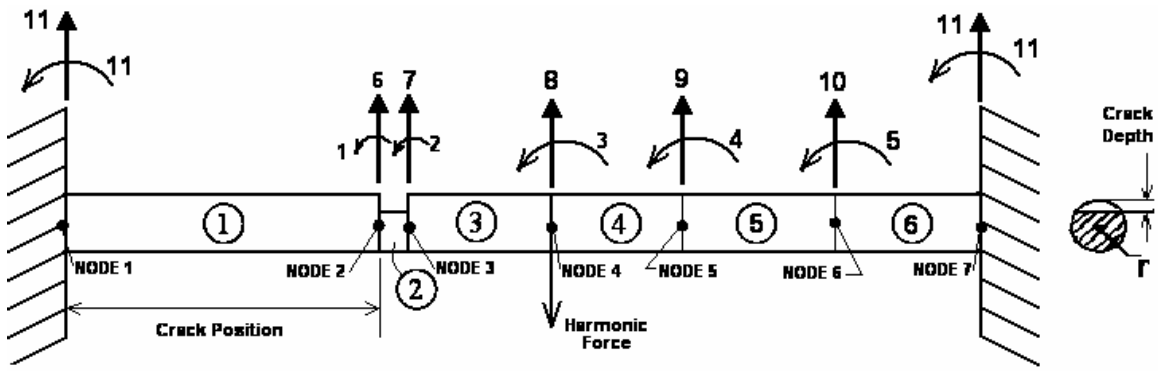

Figure 17. Fixed shaft divided in six elements and its nodal coordinates

4.3.1 Assembly of the System Stiffness Matrix

After establishing the stiffness equations for a uniform beam element, the relation between nodal displacement and nodal forces and moments is established for the entire structure considering the crack as a small element as shown in the Figure 17. The crack is represented by the element two, which has different second moment of inertia from the other elements as shown in the next figure for the cracked and uncracked shaft:

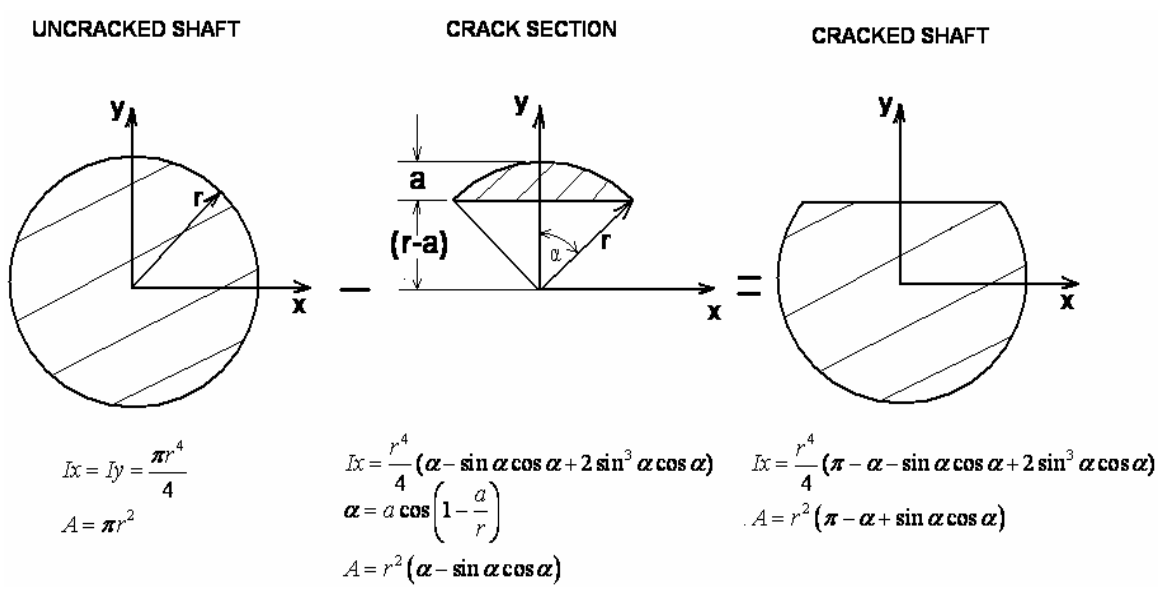

Figure 18 Second moments of inertia of the cracked and uncracked shaft

In order to increase the deflection of the rotating shaft, there was selected a plastic shaft of Acetal Delrin with the properties indicated in Table 1.

The stiffness matrix for each element is obtained systematically using the equation (99) and the corresponding indexes are assigned in order to obtain the system stiffness coefficients of the system as follows

$$
k_{(1)} = \frac{EI_1}{L_1^3}\begin{array}{c} \begin{array}{cccc} \mathbf{11} & \mathbf{11} & \mathbf{6} & \mathbf{1} \end{array} \\ \begin{bmatrix} 12 & 6L_1 & -12 & 6L_1 \\ 6L_1 & 4L_1^2 & -6L & 2L_1^2 \\ -12 & -6L_1 & 12 & -6L_1 \\ 6L_1 & 2L_1^2 & -6L_1 & 4L_1^2 \end{bmatrix} \end{array} \begin{array}{c} \mathbf{11} \\ \mathbf{11} \\ \mathbf{6} \\ \mathbf{1} \end{array}
\quad
k_{(2)} = \frac{EI_2}{L_2^3}\begin{array}{c} \begin{array}{cccc} \mathbf{6} & \mathbf{1} & \mathbf{7} & \mathbf{2} \end{array} \\ \begin{bmatrix} 12 & 6L_2 & -12 & 6L_2 \\ 6L_2 & 4L_2^2 & -6L & 2L_2^2 \\ -12 & -6L_2 & 12 & -6L_2 \\ 6L_2 & 2L_2^2 & -6L_2 & 4L_2^2 \end{bmatrix} \end{array} \begin{array}{c} \mathbf{6} \\ \mathbf{1} \\ \mathbf{7} \\ \mathbf{2} \end{array}
\quad
k_{(3)} = \frac{EI_3}{L_3^3}\begin{array}{c} \begin{array}{cccc} \mathbf{7} & \mathbf{2} & \mathbf{8} & \mathbf{3} \end{array} \\ \begin{bmatrix} 12 & 6L_3 & -12 & 6L_3 \\ 6L_3 & 4L_3^2 & -6L & 2L_3^2 \\ -12 & -6L_3 & 12 & -6L_3 \\ 6L_3 & 2L_3^2 & -6L_3 & 4L_3^2 \end{bmatrix} \end{array} \begin{array}{c} \mathbf{7} \\ \mathbf{2} \\ \mathbf{8} \\ \mathbf{3} \end{array}
$$

$$
k_{(4)} = \frac{EI_4}{L_4^3}\begin{array}{c} \begin{array}{cccc} \mathbf{8} & \mathbf{3} & \mathbf{9} & \mathbf{4} \end{array} \\ \begin{bmatrix} 12 & 6L_4 & -12 & 6L_4 \\ 6L_4 & 4L_4^2 & -6L & 2L_4^2 \\ -12 & -6L_4 & 12 & -6L_4 \\ 6L_4 & 2L_4^2 & -6L_4 & 4L_4^2 \end{bmatrix} \end{array} \begin{array}{c} \mathbf{8} \\ \mathbf{3} \\ \mathbf{9} \\ \mathbf{4} \end{array}
\quad
k_{(5)} = \frac{EI_5}{L_5^3}\begin{array}{c} \begin{array}{cccc} \mathbf{9} & \mathbf{4} & \mathbf{10} & \mathbf{5} \end{array} \\ \begin{bmatrix} 12 & 6L_5 & -12 & 6L_5 \\ 6L_5 & 4L_5^2 & -6L & 2L_5^2 \\ -12 & -6L_5 & 12 & -6L_5 \\ 6L_5 & 2L_5^2 & -6L_5 & 4L_5^2 \end{bmatrix} \end{array} \begin{array}{c} \mathbf{9} \\ \mathbf{4} \\ \mathbf{10} \\ \mathbf{5} \end{array}
\quad
k_{(6)} = \frac{EI_6}{L_6^3}\begin{array}{c} \begin{array}{cccc} \mathbf{10} & \mathbf{5} & \mathbf{11} & \mathbf{11} \end{array} \\ \begin{bmatrix} 12 & 6L_6 & -12 & 6L_6 \\ 6L_6 & 4L_6^2 & -6L & 2L_6^2 \\ -12 & -6L_6 & 12 & -6L_6 \\ 6L_6 & 2L_6^2 & -6L_6 & 4L_6^2 \end{bmatrix} \end{array} \begin{array}{c} \mathbf{10} \\ \mathbf{5} \\ \mathbf{11} \\ \mathbf{11} \end{array}
\tag{102}
$$

The system stiffness matrix is

$$
K = \begin{bmatrix}
\text{(k1(4,4)+k2(2,2))} & \text{k2(4,2)} & 0 & 0 & 0 & \text{(k1(3,4)+k2(1,2))} & \text{k2(3,2)} & 0 & 0 & 0 \\
\text{k2(2,4)} & \text{(k2(4,4)+k3(2,2))} & \text{k3(4,2)} & 0 & 0 & \text{k2(1,4)} & \text{(k2(3,4)+k3(1,2))} & \text{k3(3,2)} & 0 & 0 \\
0 & \text{k3(2,4)} & \text{(k3(4,4)+k4(2,2))} & \text{k4(4,2)} & 0 & 0 & \text{k3(1,4)} & \text{(k3(3,4)+k4(1,2))} & \text{k4(3,2)} & 0 \\
0 & 0 & \text{k4(2,4)} & \text{(k4(4,4)+k5(2,2))} & \text{k5(4,2)} & 0 & 0 & \text{k4(1,4)} & \text{(k4(3,4)+k5(1,2))} & \text{k5(3,2)} \\
0 & 0 & 0 & \text{k5(2,4)} & \text{(k5(4,4)+k6(2,2))} & 0 & 0 & 0 & \text{k5(1,4)} & \text{(k5(3,4)+k6(1,2))} \\
\text{(k1(4,3)+k2(2,1))} & \text{k2(4,1)} & 0 & 0 & 0 & \text{(k1(3,3)+k2(1,1))} & \text{k2(3,1)} & 0 & 0 & 0 \\
\text{k2(2,3)} & \text{(k2(4,3)+k3(2,1))} & \text{k3(4,1)} & 0 & 0 & \text{k2(1,3)} & \text{(k2(3,3)+k3(1,1))} & \text{k3(3,1)} & 0 & 0 \\
0 & \text{k3(2,3)} & \text{(k3(4,3)+k4(2,1))} & \text{k4(4,1)} & 0 & 0 & \text{k3(1,3)} & \text{(k3(3,3)+k4(1,1))} & \text{k4(3,1)} & 0 \\
0 & 0 & \text{k4(2,3)} & \text{(k4(4,3)+k5(2,1))} & \text{k5(4,1)} & 0 & 0 & \text{k4(1,3)} & \text{(k4(3,3)+k5(1,1))} & \text{k5(3,1)} \\
0 & 0 & 0 & \text{k5(2,3)} & \text{(k5(4,3)+k6(2,1))} & 0 & 0 & 0 & \text{k5(1,3)} & \text{(k5(3,3)+k6(1,1))}
\end{bmatrix}
\tag{103}
$$

4.3.2 System Mass Matrix

After evaluating the elemental mass coefficients the entire system is assembled exactly in the same procedure as the stiffness matrix for the system giving:

$$
M=\begin{bmatrix}
(m1(4,4)+m2(2,2)) & m2(4,2) & 0 & 0 & 0 & (m1(3,4)+m2(1,2)) & m2(3,2) & 0 & 0 & 0 \\
m2(2,4) & (m2(4,4)+m3(2,2)) & m3(4,2) & 0 & 0 & m2(1,4) & (m2(3,4)+m3(1,2)) & m3(3,2) & 0 & 0 \\
0 & m3(2,4) & (m3(4,4)+m4(2,2)) & m4(4,2) & 0 & 0 & m3(1,4) & (m3(3,4)+m4(1,2)) & m4(3,2) & 0 \\
0 & 0 & m4(2,4) & (m4(4,4)+m5(2,2)) & m5(4,2) & 0 & 0 & m4(1,4) & (m4(3,4)+m5(1,2)) & m5(3,2) \\
0 & 0 & 0 & m5(2,4) & (m5(4,4)+m6(2,2)) & 0 & 0 & 0 & m5(1,4) & (m5(3,4)+m6(1,2)) \\
(m1(4,3)+m2(2,1)) & m2(4,1) & 0 & 0 & 0 & (m1(3,3)+m2(1,1)) & m2(3,1) & 0 & 0 & 0 \\
m2(2,3) & (m2(4,3)+m3(2,1)) & m3(4,1) & 0 & 0 & m2(1,3) & (m2(3,3)+m3(1,1)) & m3(3,1) & 0 & 0 \\
0 & m3(2,3) & (m3(4,3)+m4(2,1)) & m4(4,1) & 0 & 0 & m3(1,3) & (m3(3,3)+m4(1,1)) & m4(3,1) & 0 \\
0 & 0 & m4(2,3) & (m4(4,3)+m5(2,1)) & m5(4,1) & 0 & 0 & m4(1,3) & (m4(3,3)+m5(1,1)) & m5(3,1) \\
0 & 0 & 0 & m5(2,3) & (m5(4,3)+m6(2,1)) & 0 & 0 & 0 & m5(1,3) & (m5(3,3)+m6(1,1))
\end{bmatrix}
\tag{104}
$$

Once global stiffness and mass matrices are constructed the equations of free motion can be written in partitioned matrix form as

$$
\left[\frac{[M_{ss}]}{[M_{ps}]}\,\middle|\,\frac{[M_{sp}]}{[M_{pp}]}\right]\left\{\frac{\{\ddot{Y}_s\}}{\{\ddot{Y}_p\}}\right\}+\left[\frac{[K_{ss}]}{[K_{ps}]}\,\middle|\,\frac{[K_{sp}]}{[K_{pp}]}\right]\left\{\frac{\{Y_s\}}{\{Y_p\}}\right\}=\left\{\frac{\{0\}}{\{0\}}\right\} \tag{105}
$$

Substituting {y}={Y}cos(ωt-θ) in the last equation results in the generalized eigen-problem

$$
\left[\frac{[K_{ss}]-\omega_i^2[M_{ss}]}{[K_{ps}]-\omega_i^2[M_{ps}]}\,\middle|\,\frac{[K_{sp}]-\omega_i^2[M_{sp}]}{[K_{pp}]-\omega_i^2[M_{pp}]}\right]\left\{\frac{\{Y_s\}}{\{Y_p\}}\right\}=\left\{\frac{\{0\}}{\{0\}}\right\} \tag{106}
$$

The first step for obtaining the natural frequencies is the elimination of the secondary coordinates {Ys} employing the Gauss-Jordan elimination. Then the equation (106) is reduced to

$$
\left[\frac{[I]}{[O]}\,\middle|\,\frac{-[\bar{T}_i]}{[\bar{D}_i]}\right]\left\{\frac{\{Y_s\}}{\{Y_p\}}\right\}=\left\{\frac{\{0\}}{\{0\}}\right\} \tag{107}
$$

The last equation can be written as

$$
\{Y_s\}=[\bar{T}_i]\{Y_p\} \tag{108}
$$

The ith modal shape {Y}i can be expressed as

$$\{Y_i\} = [T_i]\{Y_p\} \quad where: \quad [T_i] = \begin{bmatrix} [\bar{T}_i] \\ \hline [I] \end{bmatrix} and \{Y\}_i = \begin{Bmatrix} \{Y_s\} \\ \hline \{Y_p\} \end{Bmatrix} \tag{109}$$

The reduced stiffness and mass matrices are calculated as

$$\left[\bar{K}\right] = \left[\bar{D}_i\right] + \omega_i^2 \left[\bar{M}_i\right] \quad and \quad \left[\bar{M}_i\right] = \left[\bar{T}_i\right]^T [M] \left[\bar{T}_i\right] \tag{110}$$

4.3.2.1 Eigen Values Estimation

The natural frequencies and modal shapes are found by solving the undamped free vibration problem, that is

$$\left[\left[\bar{K}_i\right] - \omega^2 \left[\bar{M}_i\right]\right]\{a\} = \{0\} \tag{111}$$

Requiring for a nontrivial solution that

$$\left|[\bar{K}] - \omega^2 [\bar{M}]\right| = 0 \tag{112}$$

Substituting in this last equation $[\bar{K}]$ and $[\bar{M}]$ respectively, and obtaining the cubic expression of the determinant in terms of ω, the first five modal frequencies of the system { ω } are found by solving the roots of the cubic equation.

4.3.2.2 Modal Shapes Estimation

The modal shapes are determined by solving two of the equations in (111) after substituting the obtained natural frequencies and letting the first element for each modal shape equal to one

$$\{a_i\} = \begin{bmatrix} 1 \\ a_{i2} \\ a_{i3} \end{bmatrix} \tag{113}$$

The modal shapes are normalized by dividing each element of the modal shapes by the corresponding values of $\sqrt{\sum m_i a_{ij}^2}$.

4.3.2.3 Modal Matrix Assemble

The normalized modal shapes are arranged in columns to form the modal matrix

$$[\Phi]_p = \left[\{a_1\}\ \{a_2\}\ \{a_3\}\right] \tag{114}$$

The modal shapes in terms of the 10 original coordinates are obtained by

$$[\Phi] = [T][\Phi]_p \tag{115}$$

4.4 The Steady State Response Estimation

The force vector of the system and the modal matrix are employed to estimate the steady state response of the shaft subjected to the harmonic force $F_0 \cos(\omega t - \theta)$ acting on the node 4 due to the unbalance disk. The force vector is assembled as follows.

$$F = \left\{0 \quad 0 \quad F_0 \cos(\omega t - \theta) \quad 0 \quad 0\right\}' \tag{116}$$

Neglecting damping and assuming $\theta = 0$, the system can be represented with the normal equation

$$\ddot{Z}_n + \omega_n^2 Z_n = P_n \cos(\omega t) \quad where \quad P_n = \sum_{i=1}^{N} \Phi^{-1} F_{0i} \tag{117}$$

Solving the nonhomegeneous ordinary differential equation (117) employing the undetermined coefficient method as explained in [26] and applying the initial conditions we have the deflection solution of the nodal coordinates in the time as follows:

$$Z_n = \frac{P_n}{\omega_n^2 - \omega^2}[\cos(\omega t) - \cos(\omega_n t)] \tag{118}$$

The deflection of the nodal coordinates are found from the transformation

$$\{y\} = [\Phi]\{Z_n\} \quad where\,[\Phi]\,is\ the\ modal\ matrix \tag{119}$$

$$\ddot{Z}_n = \frac{Pn}{(\omega_n^2 - \omega^2)}[\omega_n^2 \cos(\omega_n t) - \omega^2 \cos(\omega t)] \tag{120}$$

$$\{\ddot{y}\} = [\Phi]\{\ddot{Z}_n\} \quad where\,[\Phi]\,is\ the\ modal\ matrix \tag{121}$$

Substituting the values of $\{Z_n\}$ into equation (119) gives the amplitudes of deflection at the nodal coordinates. The second derivative corresponds to the amplitudes of acceleration at the nodal coordinates, equation (121).

4.5 Results from the Finite Element Model

Three sets of data were considered for the simulation as shown in Table 2 : Case 1 and 2 where considered for the neural network architecture selection. Case 3 was considered for evaluate the predictive neural network performance.

Table 2. Simulation Data Sets

CASE	# Crack Depths	Crack Depth Increment [mm]	# Crack Positions	Crack Position Increment [mm]	Driving Frequency [Hz]	Total Number of Data
1	4	1.19	9	12.7	4.8	36
2	4	1.19	6	25.4	4.8	24
3	4	1	6	25.4	4.8	24

Both; mechanical properties of the shaft (taken from the technical chart of the fabricant) and geometrical properties were given as indicated in the Table 1. Simulation study was conduced developing a code in Matlab 7.1 and the Signal Processing Toolbox. The driving frequency of 4.8 Hz was taken as close to the first natural frequency as possible, but within the rage of sensitivity of the accelerometer for all cases.

4.5.1 Changes of the Vibration Parameters

The first three natural frequencies of the uncracked shaft were estimated with the finite element model giving 10 Hz, 34.6 Hz and 72.3 Hz respectively. In this study only the first mode of vibration was considered. Figure 19 (a) and (b) show how the first natural frequency decreases at

different crack scenarios, also how crack position is more sensitive to frequency reduction than crack depth.

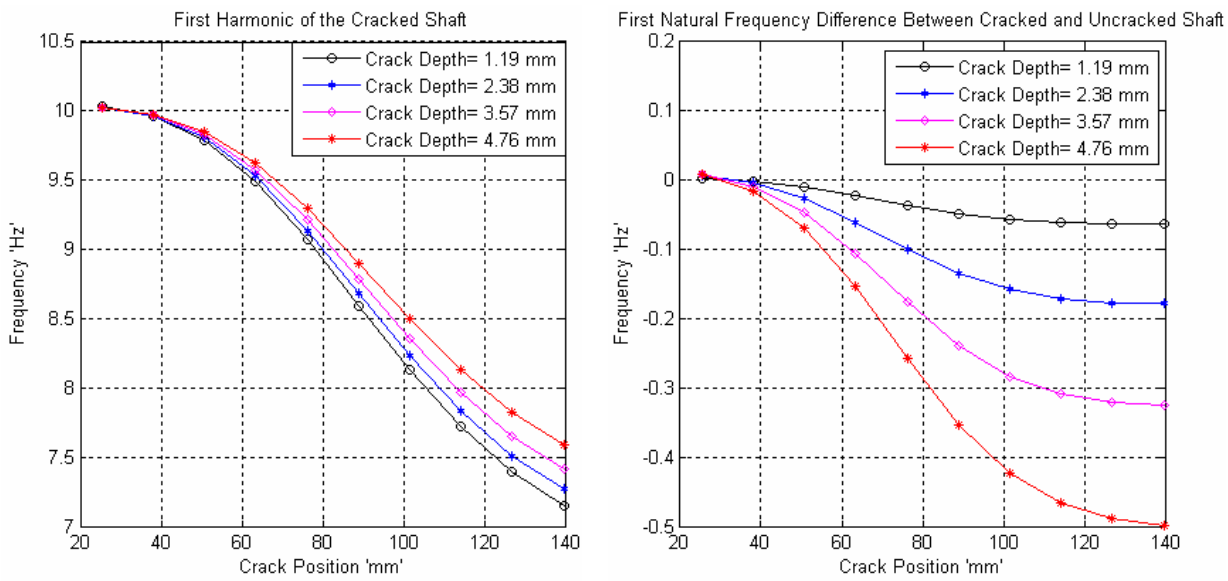

(a) (b)

Figure 19. Change in frequency for different crack depths and positions (a) First harmonic (b) Frequency difference between cracked and uncracked shaft

The following plots show how the vibration parameters: mode shapes, acceleration amplitudes and its corresponding PSDAA change between the cracked and uncracked shaft at the nodal coordinates. 7 connectivity nodes were considered numbered from left to right as shown in Figure 17. Nodes 2 and 3 were moved with the crack position and the rest remained at the same position for the simulation.

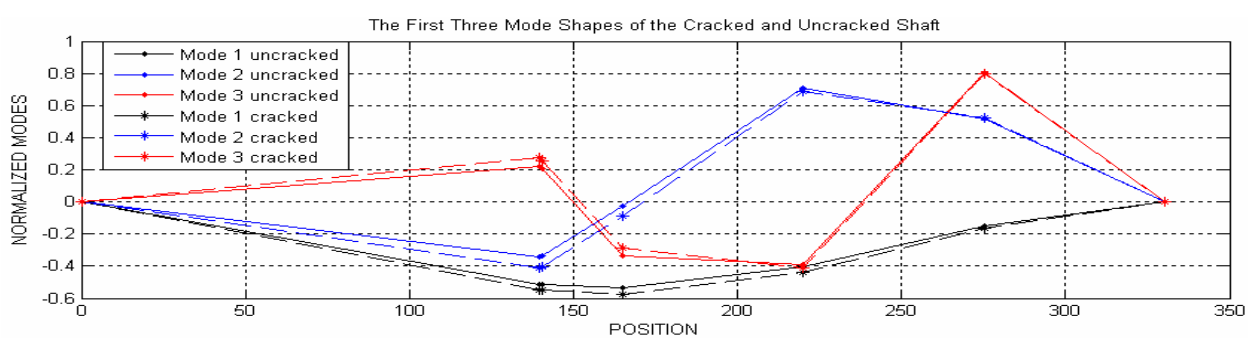

Figure 20. Mode Shapes of the shaft with crack depth =4.76 mm, crack position =140 mm

Dashed lines represent the cracked shaft and continuous lines represent the uncracked shaft. Nodes 4, 5 and 6 were considered the places for extracting the amplitudes of acceleration from the shaft.

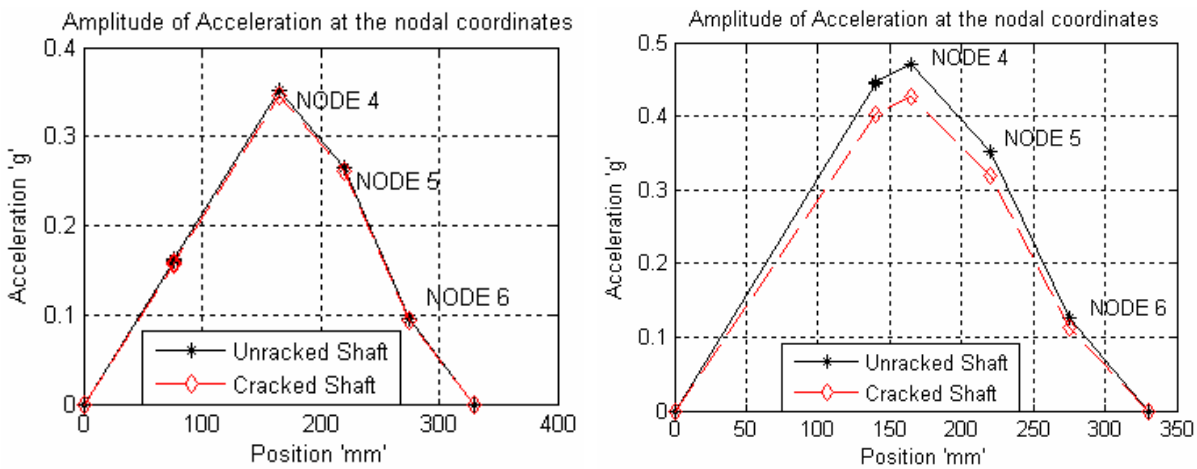

(a) (b)

Figure 21. Amplitude of acceleration at the nodal coordinates of the shaft with crack depth =4.76 mm at 4.8 Hz driving frequency (a) crack position=76 mm (b) crack position =140 mm

The following plots show two acceleration signals in the time obtained from the analytical model from nodes 4 and 6. Figure 22 (b) shows how amplitude of acceleration response decreases with the presence of crack and how this change increases when the crack approaches to the middle.

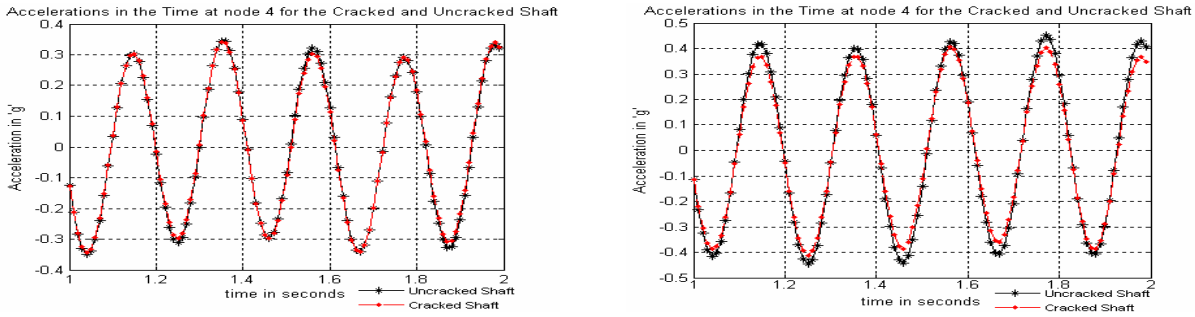

(a) (b)

Figure 22. Acceleration of the shaft at node 4 with crack depth =4.76 mm and a driving frequency of 4.8 Hz (a) crack position=76 mm (b) crack position =140 mm

The auto spectral density frequency response amplitudes at three nodes of the structure were taken as the vibrating parameters as shown in the next figures for signal simulated at the node 4 at two different crack positions:

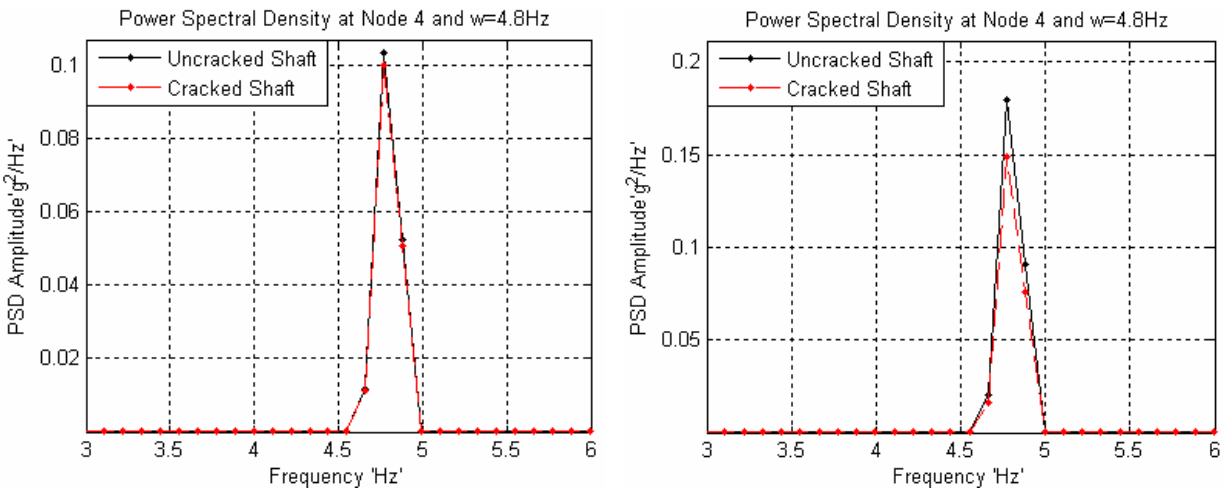

(a) **(b)**

Figure 23 PSD of acceleration signals at node 4 for the shaft with crack depth =4.76 mm and driving frequency of 4.8 Hz (a) Crack at 76 mm (b) Crack at 140 mm

The following plot shows the behavior of the PSD frequency response amplitude difference between the cracked and uncracked shaft for different crack depths and positions.

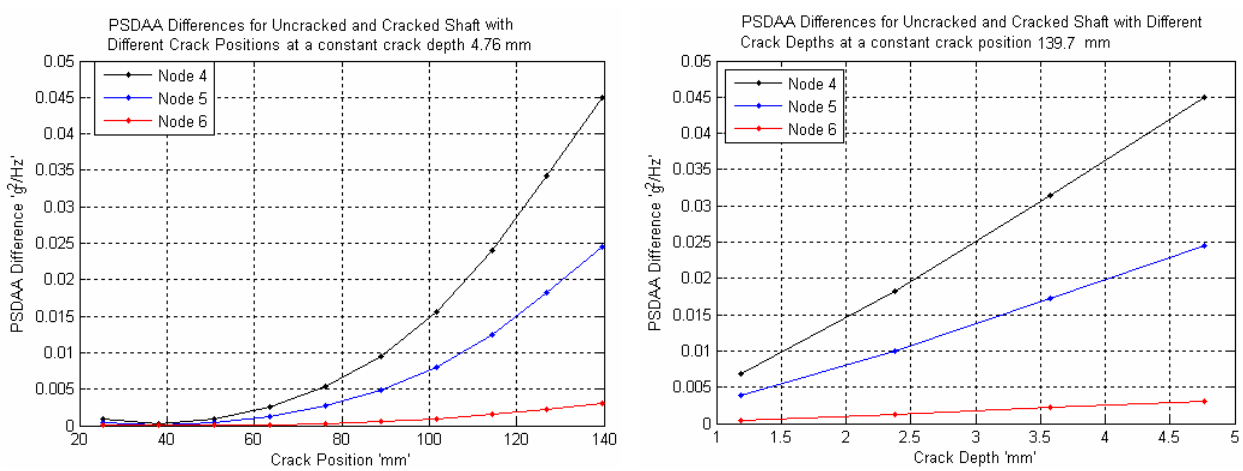

(a) (b)

Figure 24 Difference in PSD-Amplitudes of acceleration for (a) Different crack positions (b) Different crack depths

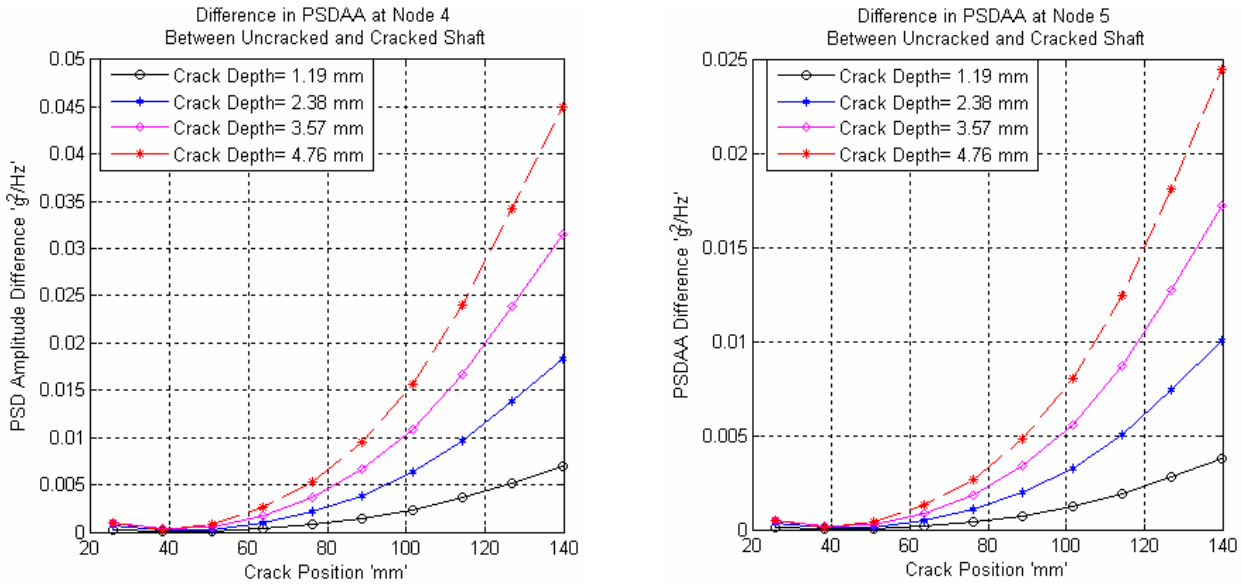

(a) (b)

Figure 25 Response Surfaces of the Power Spectral Density Difference between Cracked and Uncracked shaft (a) Node 4 and (b) Node 5

Simulated results obtained by the finite element method shown in Figure 24 and Figure 25 demonstrate the uniqueness of the amplitudes of the power spectral densities difference between cracked and uncracked shaft for different crack depths and positions within a range of 63-140 mm. However, very low sensitivity results were obtained when the crack approached to the fixed end of the shaft within the range of 25.4 - 63 mm for the three nodes evaluated.

5 Identification of Crack Size and Location Based on Neural Networks Method

Multilayer feedforward neural networks with Backpropagation algorithm were employed in this study as a non linear function approximator to establish a relationship between input vectors and target values. MATLAB 7.1 Neural Network Toolbox functions were used for developing the four steps of the Backpropagation training: Assemble of the training data, creation of the neural network object, training the network, simulating the network to new inputs. The performance of the network is measured by comparing the output of the network with the corresponding target value.

The Backpropagation algorithm is an extension of the steepest descendent algorithm in which the performance index is the mean square error, and can be used to train multilayer networks for minimizing the squared error. The Backpropagation algorithm uses the chain rule in order to compute the derivatives of the squared error with respect to the weights and biases in the hidden layers. It is called Backpropagation because the derivatives are computed first at the last layer of the network, and then propagated backward through the network, using the chain rule, to compute the derivatives in the hidden layers.

The index that measures the neural network performance is given by the mean squared error. The algorithm should adjust the network parameters in order to minimize the mean square error:

$$F(x) = E[e^2] = E[(t-a)^2] \tag{122}$$

Where x is the vector of network weights and biases, E is the expectation and e is the error vector defined as the difference between the targets and the output of the network. For multiple outputs this generalizes:

$$F(x) = E[e^T e] = E[(t-a)^2 (t-a)] \tag{123}$$

The expectation of the squared error is replaced by the squared error at iteration k as follows:

$$\hat{F}(x) = (t(k) - a(k))^T (t(k) - a(k)) = e^T(k) e(k) \tag{124}$$

A neural network is trained when the learning algorithm find the weight matrices and bias vector in such way that the $\hat{F}(x)$ at the kth iteration is minimized.

The Backpropagation training algorithm has the following steps:

1. The input propagated forward through the network:

$$a^0 = P \tag{125}$$

$$a^{m+1} = f^{m+1}(W^{m+1}a^m + b^{m+1}) \ \ for\ m = 0,1,...,M-1 \tag{126}$$

$$a = a^M \tag{127}$$

2. The sensitivities are propagated backward through the network.

- First the last layer sensitivity is computed:

$$s^M = -2\dot{F}(n^M)(t-a) \tag{128}$$

- The other sensitivities are computed by backpropagating the sensitivity of the last layer:

$$s^m = \dot{F}^m(n^m)(W^{m+1})^T s^{m+1},\ for\ m = M-1,...,2,1. \tag{129}$$

3. The weights and biases are updated using the approximate steepest descendent rule:

$$\begin{gathered} W^m(k+1) = W^m(k) - \alpha s^m (a^{m-1})^T \\ b^m(k+1) = b^m(k) - \alpha s^m \\ m = number\ of\ layer, k = iteration\ number, \alpha = learning\ rate \end{gathered} \tag{130}$$

Last iteration process stops when until the difference of the network response and data selected for training reaches some acceptable level.

5.1.1 Assemble of the training data

Known inputs P and targets T were obtained first theoretically by the simulation with finite element method and then experimentally employing the wireless accelerometer. The input vector (P) was created from the difference in the amplitudes of acceleration response between cracked and uncracked shaft at nodes 4, 5 and 6. Target matrices (T) were constructed by considering

known locations and depths of the crack to be associated to the pattern of amplitudes of acceleration response differences.

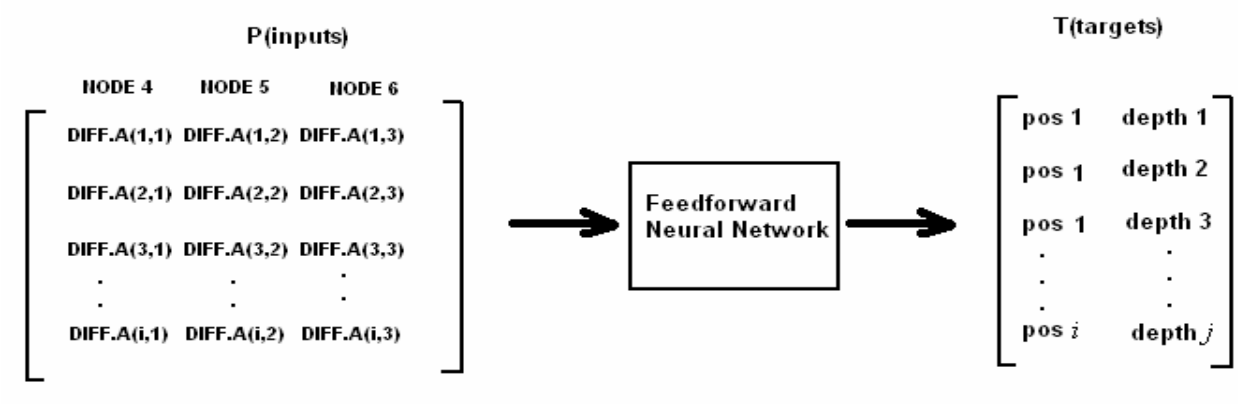

Figure 26. Training data sets: Inputs = (amplitudes of acceleration frequency response at nodes 4, 5 and 6, and Outputs = (crack positions and depths)

There was considered two sizes for the input matrices and target vectors for training in order to determine its significance in the performance of the network: one with 6 positions and 4 depths for 24 total points and another with 9 positions and 4 depths for 36 total points.

5.1.2 Creation of the Neural Network Object

A network with two layers was studied considering that for a network to be able to generalize, it should have fewer parameters than the data points used for training, and that it have been shown that two layer networks with a nonlinear transfer function in the hidden layer and a linear transfer function in the output layer can approximate virtually any function of interest to any degree of accuracy as established by Hagan [6].

A factorial experimental design was performed to identify the parameters that affect the performance of the nonlinear response of the network in order to find the rules for the neural network model identification. This technique was based on the study made by Ramirez Beltran [21]. A three factorial design was developed considering: (1) the number of input points that will be used for training the network within 2 levels: 24 and 36 points, which corresponds to 6 and 9 crack positions with 4 crack depths.(2) the type of transfer function used in the hidden layer considering 2 levels for this qualitative factor: a Sigmoidal and a Hyperbolic Tangent transfer

function, and (3) the number of neurons in the hidden layer, considering 8 levels for this factor. The transfer functions employed in the hidden layer were:

$$Sigmoidal\ function: f_1(n) = \frac{1}{1+e^{-n}} \quad Tangent\ function: f_2(n) = \frac{e^n - e^{-n}}{e^n + e^{-n}} \qquad \textbf{(131)}$$
$$n = network\ input$$

Simulated data obtained by the finite element model where used first for training and then for testing the network. Deviations in crack depth and crack position were integrated in one variable named "Total Error" which was defined as the square root of the summation of the squared errors. The "Total Error" was assumed as the response variable of the system, which were treated for the analysis of variance (ANOVA). Five replications were obtained for each treatment combination for a total of (2)x(2)x(8)x(5)=160 experiments. The experiment was conducted to establish statistically the rules to identify the structure of the network. Matlab 7.1 and the neural networks toolbox functions were employed to develop a code for training the network with the Backpropagation algorithm. Experiment results in Table 3 corresponding to the analysis of variance made in Minitab 14 shown that the performance of the network depends simultaneously on the number of data, number of neurons and the interaction of both.

Table 3. Analysis of variance for the Total Error of the simulated data

Source	DF	Seq SS	Adj SS	Adj MS	F	P
NumData	1	24.764	24.764	24.764	19.98	0
Function	1	0.109	0.109	0.109	0.09	0.768
Neurons	7	81.319	81.319	11.617	9.37	0
NumData*Function	1	0.006	0.006	0.006	0.01	0.942
NumData*Neurons	7	34.646	34.646	4.949	3.99	0.001
Function*Neurons	7	20.221	20.221	2.889	2.33	0.029
NumData*Function*Neurons	7	11.168	11.168	1.595	1.29	0.262
Error	128	158.664	158.664	1.24		
Total	159	330.898				

Next figures show that performance of the network is good when only few neurons and higher set of training data are used, whereas, poor consistency is exhibited when a large number of neurons are used.

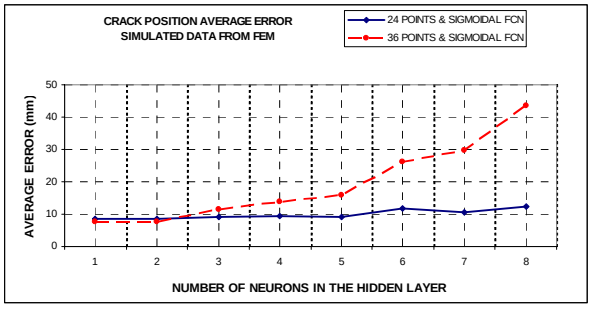

(a)

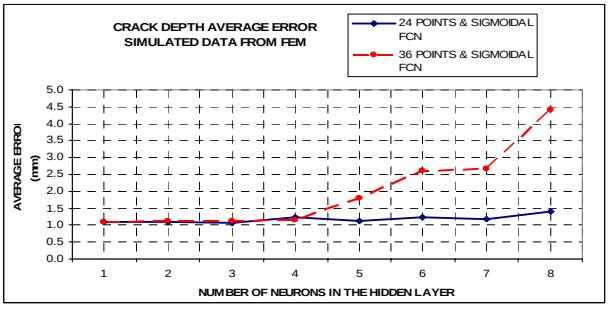

(b)

Figure 27. Predicted average error from simulated data (a) Crack position with a sigmoidal transfer function (b) Crack depth with sigmoidal transfer function

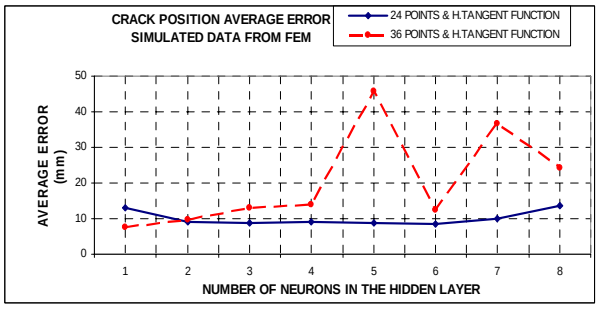

(c)

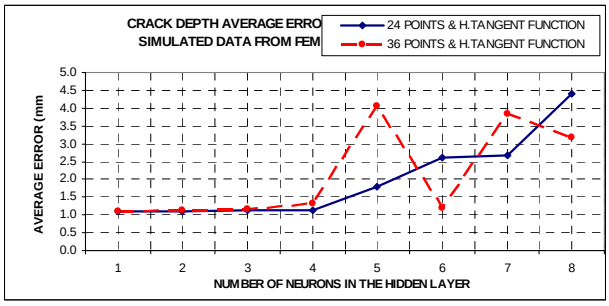

(d)

Figure 28. Predicted average error from simulated data (c) Crack position with a hyperbolic tangent function (d) Crack depth with a hyperbolic tangent function

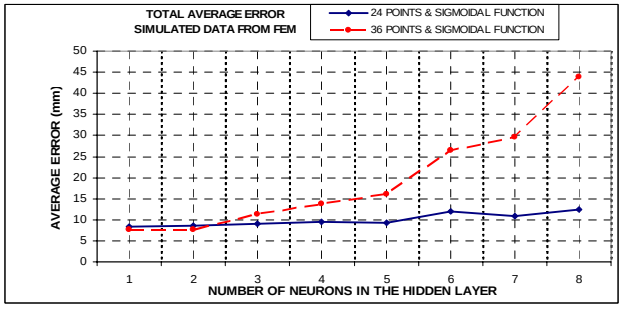

(e)

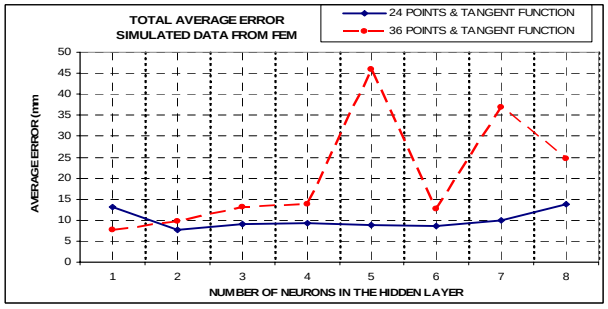

(f)

Figure 29. Predicted average error from simulated data (e) Predicted total error with Sigmoidal transfer function (f) Predicted total error with Hyperbolic tangent transfer function

Simulating results indicate that the best structure is the one that reveals the lowest average error with the smallest number of neurons, therefore a single neuron in the hidden layer was considered with a sigmoidal transfer function for the network with one input vector P of 3 x 1 with three differences in amplitude of acceleration spectral densities: P1,P2 and P3 , and two neurons with linear transfer functions in the output layer that give the output vector a corresponding to crack depth and position.

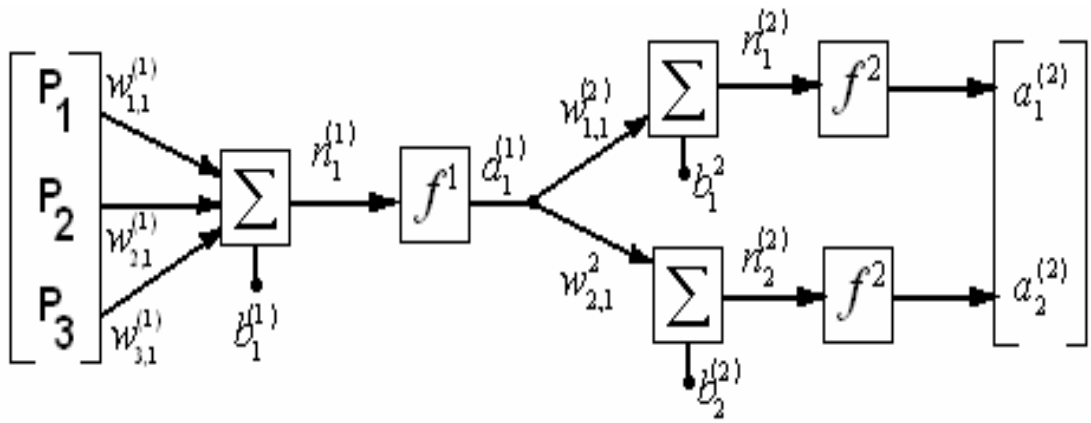

Figure 30. Neural network structure for the predictive model with simulated data

The icons and notation presented in this figure were taken from Hagan [6], where W(m) represents the weight matrix of the mth layer, b(m) is the bias vector of the mth layer, n(m) is the net input vector to the network in the mth layer, a(m) is the net output of the network in the mth layer. Thus the output of the network can be expressed by the following nested function:

$$a^{(2)} = f^{(2)}\{w^{(2)} f^{(1)}(w^{(1)}P + b^{(1)}) + b^{(2)}\} \quad \textbf{(132)}$$

The output of the predictive network is $a^{(2)}$, and $f^{(m)}$ is the transfer function of the mth layer.

New simulated data unknown for the selected network was tested with the selected neural network and the performance is shown in the next figures:

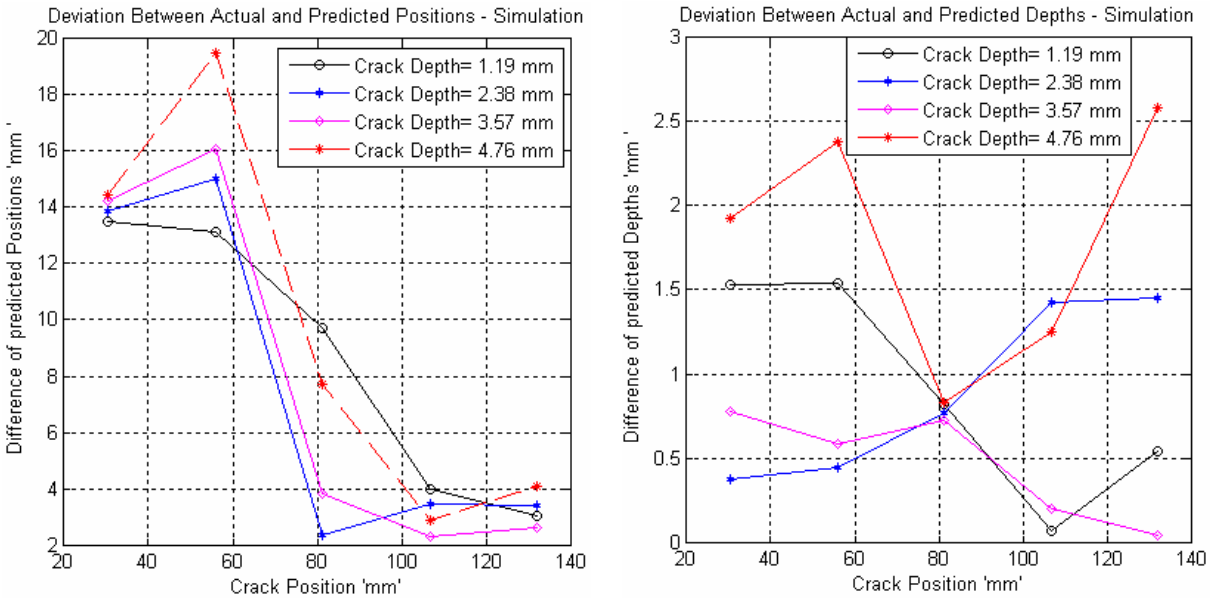

(a) (b)

Figure 31. Performance of the network predictor (a) Crack positions (b) Crack depths

Figure 31 shows higher differences in crack position predictions close to the shaft support. This behavior can be attributed to the low sensitivity of the vibration parameters obtained in the simulating experiment.

Next table summarizes the performance of the selected artificial neural network:

Table 4. Performance of the neural network for the simulating data

NEURAL NETWORK PERFORMACE (IN MILIMETERS)					
Average error in positon	Minimal error in position	Maximal error in position	Average error in depth	Minimal error in depth	Maximal error in depth
7.2119	0.0178	16.8989	0.6578	0.1257	2.0365

6 Experimental Study

Experimental modal analysis was used in this research to extract differences in magnitude of the spectral density of acceleration frequency response from the linear and time invariant rotating shaft working at a constant driving frequency below the first harmonic. Extracted data were arranged in matrices and introduced into the Neural Network model to solve the inverse problem of relating the acceleration amplitude frequency responses at three different positions of the shaft with the failure characteristics: crack depth and position. The process of determining the amplitudes of the frequency response from the experimental model involved signal processing and random signal analysis.

6.1 Signal Processing

The primary concern of signal processing is the conversion of the analog signals of the accelerometer into a corresponding sequence of digital values that accurately describe the time varying characteristics of the inputs to, and responses from the system.

6.1.1 The Fast Fourier Transform

Once the digital record of the signal is available, the discrete version of the Fourier transform is performed to transform the data from time domain to the frequency domain. This transform provides a series of discrete time history value by accomplishing the series defined by

$$x_{(t_k)} = \frac{a_0}{2} + \sum_{i=1}^{N/2} (a_i \cos(\frac{2\pi i t_k}{T}) + b_i \sin(\frac{2\pi i t_k}{T}) \qquad k = 1, 2, ...N \qquad \textbf{(133)}$$

Where the digital coefficients are given by

$$a_0 = \frac{1}{N}\sum_{k=1}^{N} x_k \qquad a_i = \frac{1}{N}\sum_{k=1}^{N} x_k \cos(\frac{2\pi i k}{N}) \qquad b_i = \frac{1}{N}\sum_{k=1}^{N} x_k \sin(\frac{2\pi i k}{N}) \qquad \textbf{(134)}$$

The software Matlab 7.1 and the signal processing toolbox were used as analyzer in this study to calculate the coefficients of equation (134) given the digital record $x_{(t_k)}$ for the measured signal. The number of samples is fixed for the analyzer and in this study N is 240 samples.

Last equations can also be written in matrix form as

$$\{x\} = [C]\{a\} \tag{135}$$

Where {x} is the vector of samples with elements $x_{(t_k)}$ and {a} is the vector of the spectral coefficients: a_0, ai and bi. The matrix C consists of elements containing the cosine and sine coefficients as indicated in equation (133). The solution of the system for the spectral coefficients is given by

$$\{a\} = [C]^{-1}\{x\} \tag{136}$$

The computation of the inverse matrix $[C]^{-1}$ is called the Fast Fourier Transform (FFT). While {x} represents the digital version, {a} represents the spectral coefficients of the frequency content of the signal response.

6.1.2 Errors

The accurate measurement of frequency response measurements depends heavily on minimizing the errors (noise) involved with the digital signal processing. These errors are generally grouped in two categories: variance and bias. The variance part of the error is due to random deviation of each sample function from the mean. Statistically, if sufficient sample measurements are evaluated (averages), the averaged estimate will closely approximate the expected function with a high degree of confidence. The bias portion of the error, on the other hand is due to a system characteristic or measure procedure consistently resulting in an incorrect estimate. The general errors are aliasing and leakage. Knowledge of the form and origin of these errors were very important in reducing the resultant effect in the frequency response amplitudes estimation.

6.1.2.1 Aliasing

A typical error introduced in digital signal processing due to an improper sampling time is called aliasing, which results from the A/D conversion and refers to the misrepresentation of the analog signal the digital record, this error is classified as bias. Since any measurement instrument is limited in time resolution, or frequency bandwidth, and if the sampling rate is too slow to catch

the details of the analog signal, the digital representation will cause high frequencies to appear as low frequencies. For the reduction of this error the sampling frequency is two times as high as the maximum natural frequency of the system as stated by the Shannon's Sampling Theorem.

$$F_{samp} = \frac{1}{\Delta t} = F_{Nyq} \cdot 2 \qquad F_{Nyq} \geq F_{\max} \tag{137}$$

The Nyquist frequency is the theoretical limit for the maximum frequency. In this study, the sampling frequency is 1000(Hz) and the natural frequency is lower than 100(Hz), therefore, this sampling frequency is high enough to reduce aliasing error and satisfy the requirement of the data acquisition.

6.1.2.2 Leakage

The leakage error is produced by the truncation of the signal in the time domain(T), which violates the condition for the Fast Fourier Transform algorithm where the periodic signal must be sampled over a finite time multiple of its period. Erroneous frequencies appear in the digital representation if the signal is cut off inside a period because the digital Fourier transform of the finite length of signal assumes that the signal is periodic within the sample record length. Thus the actual frequency will "leak" into a number of fictitious frequencies.

This problem can be reduced by using a window function, which involves multiplying the original signal by a weighting signal to be zero outside the sampling period. In this study Hanning window is employed using the software Matlab 7.1.

6.2 Wireless Sensor Development

An accelerometer ADXL202E with duty cycle output was conditioned to work wireless by means of the transmitter TXM-418-LC and the receiver RXM-418-LC-C. The accelerometer used is capable of measuring positive and negative absolute accelerations at least +/- 2g. The sensor is a surface micro-machined polysilicon structure built on top of silicon waffer. Polysilicon springs suspended the structure over the surface of the waffer and provoke a resistance against acceleration forces. Deflection of the structure is measured using a differential capacitor that consists of independent fixed plates and central plates attached to the moving mass

as shown in the Figure 32 (a). The resulting output is a square wave whose amplitude is proportional to acceleration as shown in the Figure 32 (b).

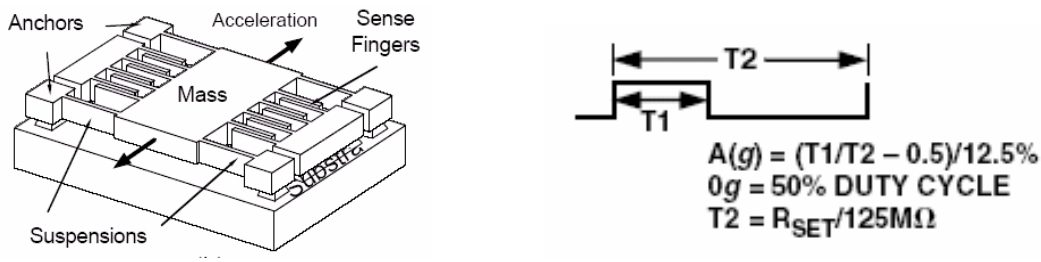

(a) (b)

Figure 32. Representation of the Accelerometer and duty cycle [3] (a) Accelerometer (b) Analog duty cycle signal

Acceleration will deflect the suspension blades and unbalance the differential capacitor. Accelerometer is made on a single IC Chip 5mm x 5 mm x 2 mm operating with voltage rage of 3V to 5.25 V DC. The photolithography technique was employed for the fabrication of the circuits. The duty cycle period was adjusted with the resistor (Rset) of 250 KΩ and the capacitors of 0.1 µF were selected as a physical low pass filter limiting frequencies over 50 Hz.

6.2.1 Circuit Design Process

In the first step the lay out of each circuit is made employing CAD software AutoCAD 2005. The circuits are distributed on the area of the presensitized PCB board to optimize the process, the connections were made in black and the background was white for all the circuits as shown and the circuits are printed on a transparence film as shown in Figure 33 which is used as a protection film for the next step of the circuit fabrication.

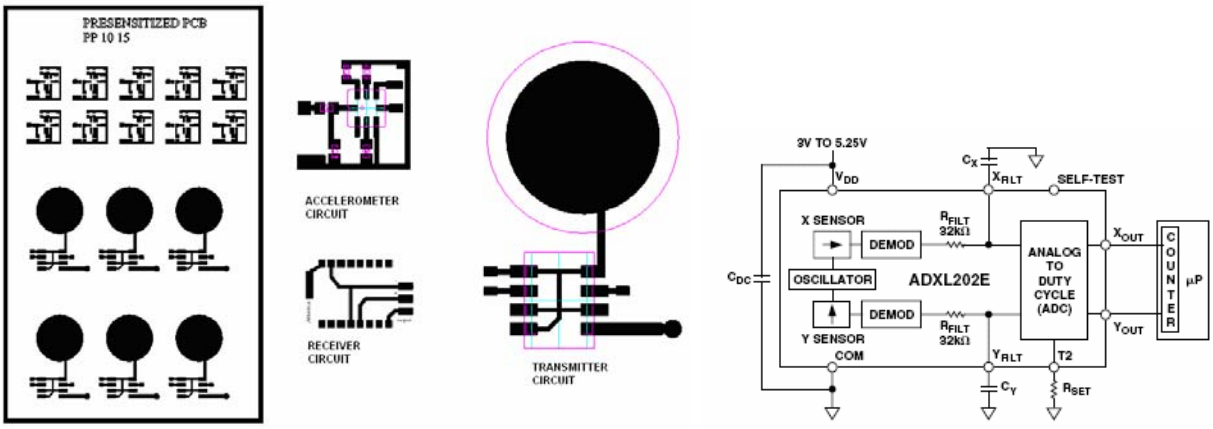

(a) (b)

Figure 33. (a) Circuit designs for the PCB (b) Accelerometer block diagram taken from [3]

6.2.2 Exposing the Pre-sensitized P.C.B

The black protection of the PCB board is removed. The board is exposed in Kinsten Exposure Box for 60-90 seconds. Circuit transparency is put on top of the board then a glass sheet in the top press them like a sandwich and the vacuum pump is turned on in order to obtain good contact between the film and the board. The UV light is turned on for 8-10 minutes.

6.2.3 Developing

The board immersed in AZ developer and deionized water. The board is held with tweezers and agitated mildly until the photoresist exposed to the UV light has been fully dissolved till the patterned part on the copper become legible, the same as the mask pattern. The board is rinsed with running water.

6.2.4 Etching

Board is etched into etchant E1-G PCB with artwork up. The board is agitated gently, till the unwanted copper foil etched away, only the circuit pattern left (It takes15-60 minutes). The board is rinsed with plenty water.

6.2.5 Soldering the Circuit

After the PCB board is ready, each circuit board is cut with a saw and then the integrated circuits are soldered according to the corresponding circuit design. The analog voltage signal of

the accelerometer shown in Figure 34 (a) is sent by the transmitter module in radio frequency waves at 418 KHz. This radio frequency signal is acquired by the receiver module shown in Figure 34 (b) and sent to the oscilloscope in parallel to the analyzer through a data acquisition board and data acquisition card as shown below in Figure 35. The signal is sampled at 10000 KHz by the acquisition board NI-6024E and the recorded data is then processed with Matlab to obtain a digital acceleration signal record.

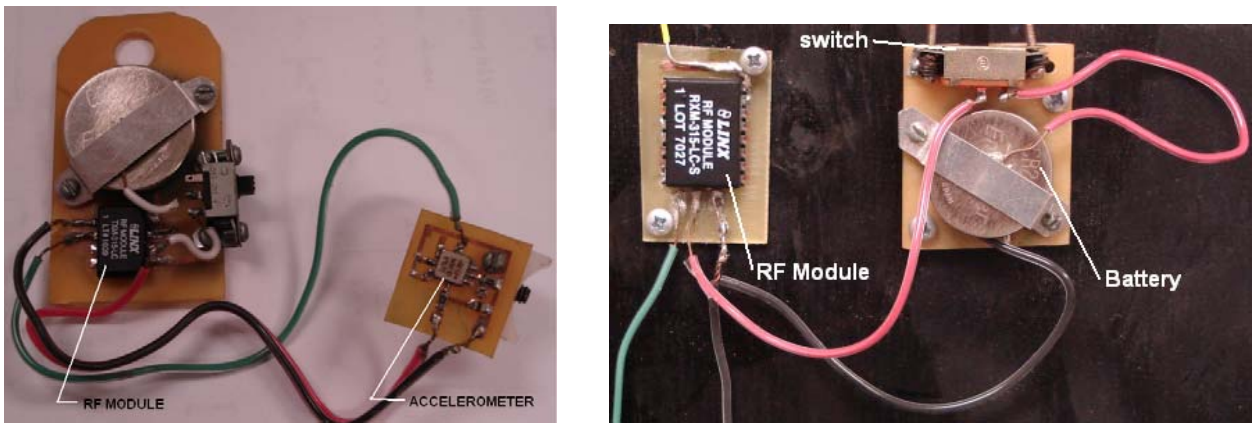

(a) (b)

Figure 34 (a) Accelerometer and transmitter circuits (b) Receiver circuit

There were developed two accelerometers working at different frequencies at the same time, but only one of them was employed in order to reduce errors coming from two different sources in the experiment.

After some tests, the shape of the antenna was modified and located closer to the fault simulator to reduce noise.

6.2.6 Sensitivity of the wireless sensor

The wireless sensor sensitivity was calculated pointing the axis directly to the earth with a help of a thin wire and a weight. The 1 g accelerometer output was saved and then the sensor was turned 180° to measure -1 g. Using the two duty cycle readings from the oscilloscope the sensitivity was estimated as:

$$Sensitivity = \left[\frac{54\% - 47\%}{2} \right] g = 3.5\% \, g \qquad \textbf{(138)}$$

6.2.7 Data Acquisition System and Experimental Setup

The data acquisition system consists of an acquisition board National Instruments CB-68LP, which connects the receiver circuit with the data acquisition board NI6024E. The data acquisition board is connected to the communication port of a processor. Analog signal is sent by the transmitter as radio frequency waves at 418 KHz, which is launched by the receiver to the data acquisition board and data acquisition card. A set of this signal is recorded by means of the data acquisition card connected to the processor. This card was configured to work with the software Matlab 7.1 and the signal processing toolbox. The signal was also monitored by a oscilloscope connected in parallel to the receiver circuit during the sampling.

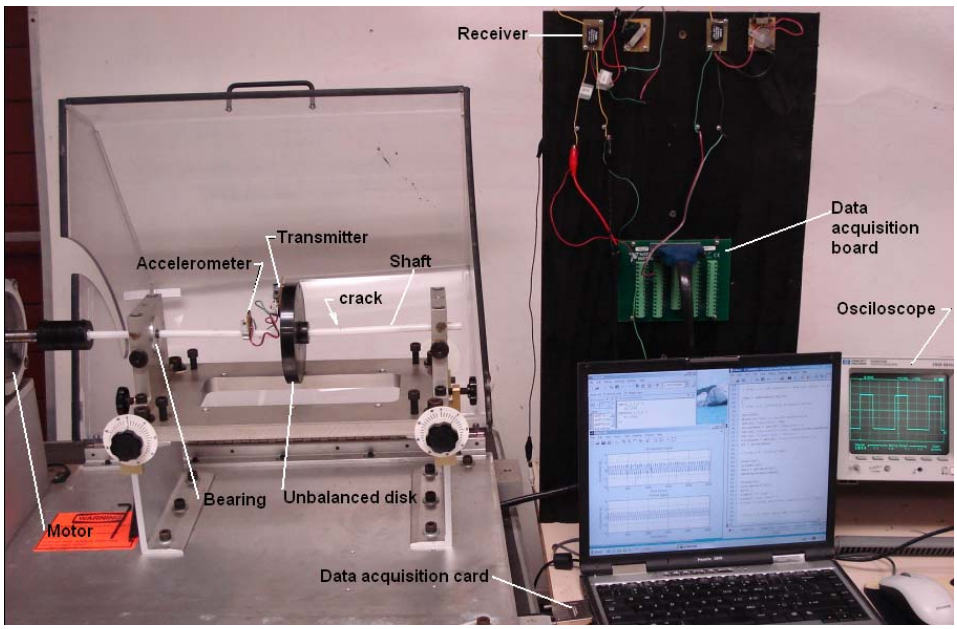

Figure 35. Data Acquisition System and Experimental Setup

The transmitter circuit is screwed to the disk and wired to the accelerometer. Both, accelerometer and transmitter rotate with the system. The receiver is connected to data acquisition hardware, which provides digital signal of the sensor to the processor. Data acquisition software Matlab 7.1 with the Signal Processing Toolbox [16] is employed to process the acceleration frequency response of the accelerometer.

Transverse cracks at different positions and sizes were machined on the Delrin shafts to complete the same cases of data sets indicated in Table 2 for the simulation study.

6.3 Experimental Results

The analog signal in terms of voltage duty cycle signal proportional to acceleration was successfully obtained from the wireless accelerometer as shown in the Figure 36 (a), this signal was conditioned and converted to digital employing a code in Matlab 7.1 to obtain the acceleration signal in the time. Figure 36 (b) shows a noisy sample in order to demonstrate the performance of the filters used for signal conditioning.

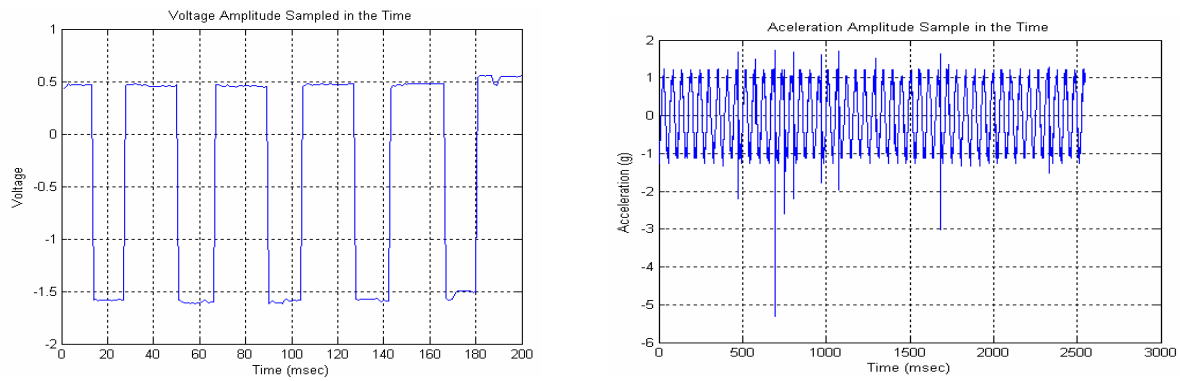

(a) (b)

Figure 36. Signal processing (a) Duty Cycle Signal (b) Acceleration Signal in the time

A capacitor of 0.05 µF working in the output of the accelerometer filters the signal from noise limiting the bandwidth to 100 Hz reducing aliasing and noise. Digital filters Sgolay and Hanning window were applied to the acceleration signal in the time to reduce noise as shown below in Figure 37(a).Then the filtered signal was brought to the frequency domain by means of the power spectral density of the acceleration as shown in the Figure 37(b).

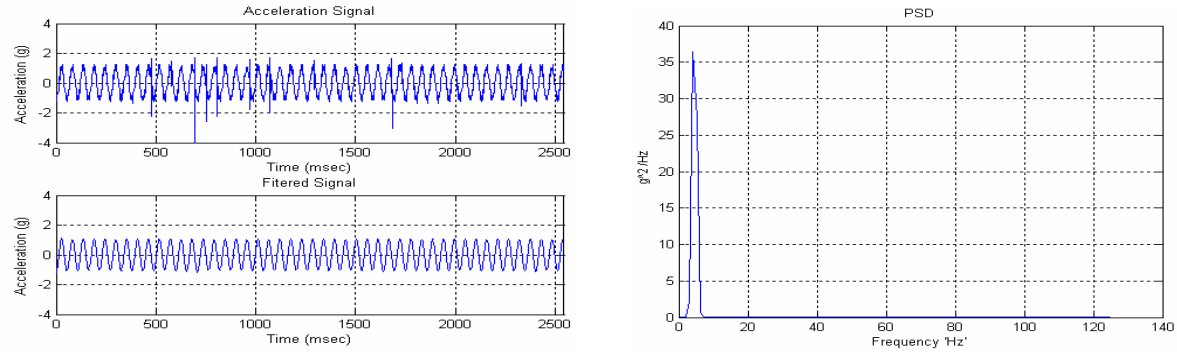

(a) (b)

Figure 37. (a) Acceleration filtered signal (b) Acceleration Power Spectral Density

Difference in PSD amplitudes for uncracked and cracked shaft at different crack depths and positions for experimental data are shown in the next figures for the nodes 4 and 5.

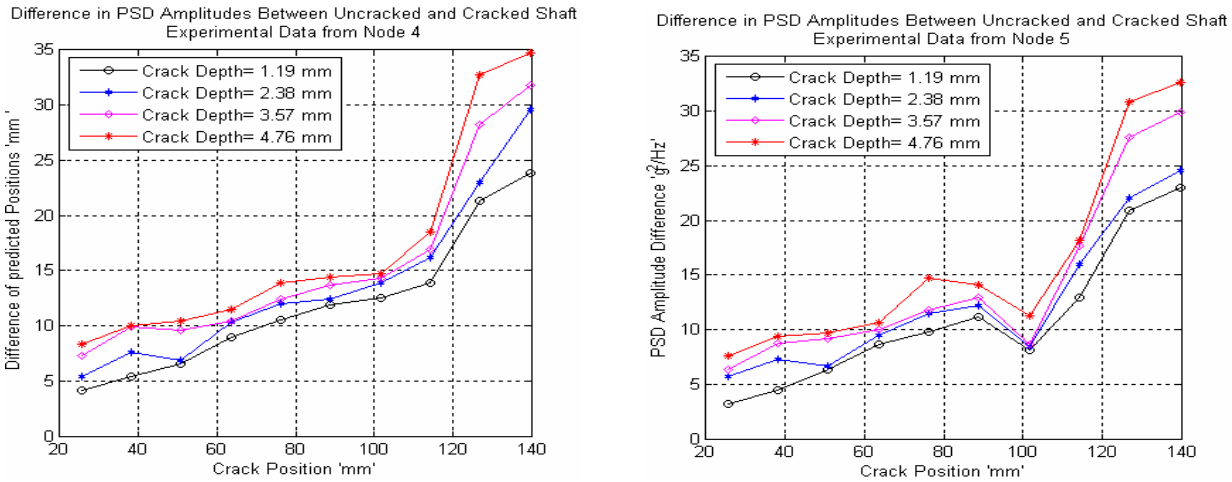

Figure 38. Experimental power spectral density amplitude differences

The differences in PSDAA between cracked and uncracked shaft at nodes 4, 5 and 6 obtained experimentally were stored as an input pattern matrix and then used for training the network that was used to predict the failure of the dynamic system for unknown data in the same manner as in the simulated part of this study. Experiment results in Table 5 corresponding to the analysis of variance made in Minitab 14 shown that the performance of the network depends simultaneously on the number of data, the transfer function, the number of neurons, the interaction of number of data with the transfer function and the interaction of number of data with number of neurons.

Table 5. Analysis of variance for the Total Error of the experimental data

Source	DF	Seq SS	Adj SS	Adj MS	F	P
NumData	1	50.1098	50.1098	50.1098	248.99	0
Function	1	4.1686	4.1686	4.1686	20.71	0
Neurons	7	6.7383	6.7383	0.9626	4.78	0
NumData*Function	1	1.4141	1.4141	1.4141	7.03	0.009
NumData*Neurons	7	21.354	21.354	3.0506	15.16	0
Function*Neurons	7	2.4587	2.4587	0.3512	1.75	0.104
NumData*Function*Neurons	7	2.5356	2.5356	0.3622	1.8	0.093
Error	128	25.7604	25.7604	0.2013		
Total	159	114.5395				

Next figures show that performance of the network is good when 5 to 7 neurons and higher set of training data are used, whereas, poor consistency is exhibited when a small number of neurons are used.

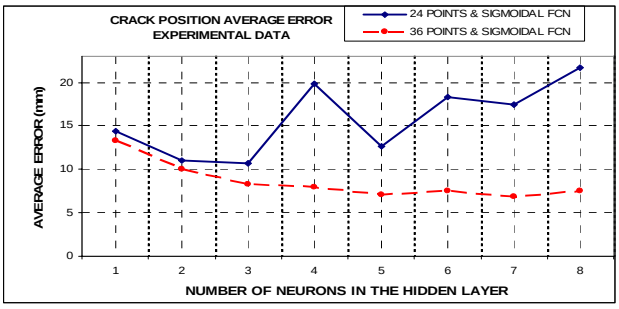

(a)

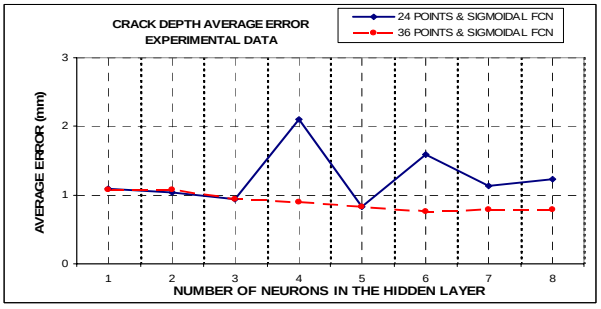

(b)

Figure 39. Predicted average error from experimental data (a) Crack position with a sigmoidal transfer function (b) Crack depth with sigmoidal transfer function

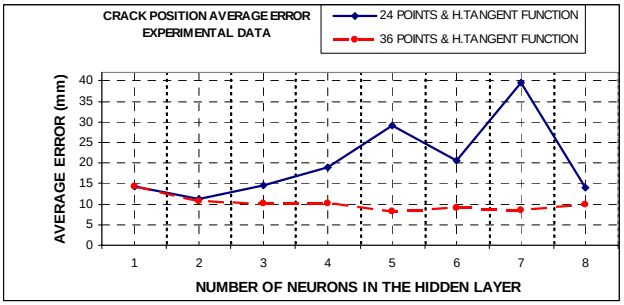

(c)

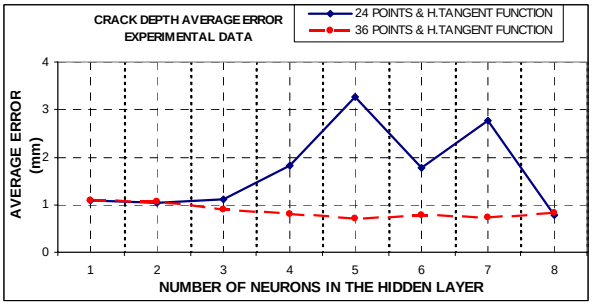

(d)

Figure 40. Predicted average error from experimental data (c) Crack position with a hyperbolic tangent function (d) crack depth with a hyperbolic tangent function

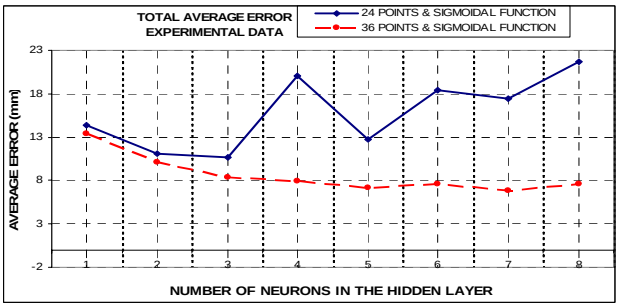

(e)

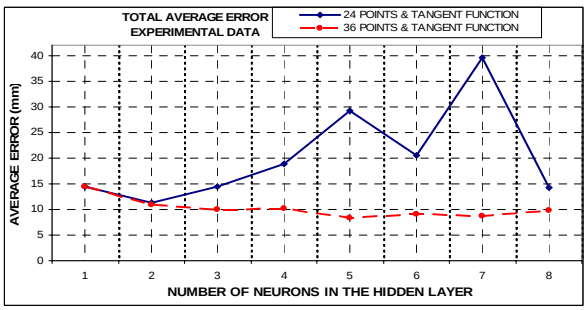

(f)

Figure 41. Predicted average error from experimental data (e) Total error with sigmoidal transfer function (f) Total error with hyperbolic tangent transfer function.

Results of the experiment indicate that the structure revealing the lowest average error with the smallest number of neurons is the one with five neurons in the hidden layer, therefore there was

considered a network with a sigmoidal transfer functions with one input vector P of 3 x 1, and two neurons with linear transfer functions in the output layer that give the output vector a corresponding to crack depth and position as shown in the next schematic.

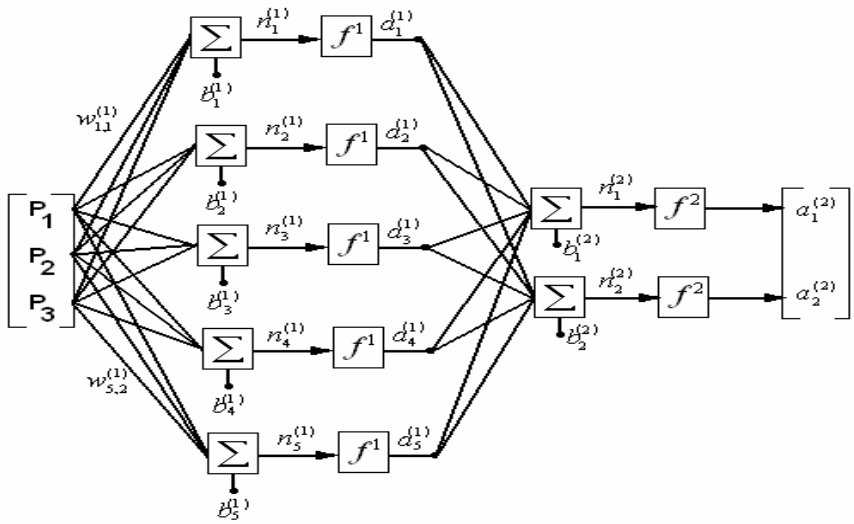

Figure 42. Neural network structure schematic for the predictive model for the experimental data

New experimental data unknown for the selected network was tested and the performance is shown in the next figures:

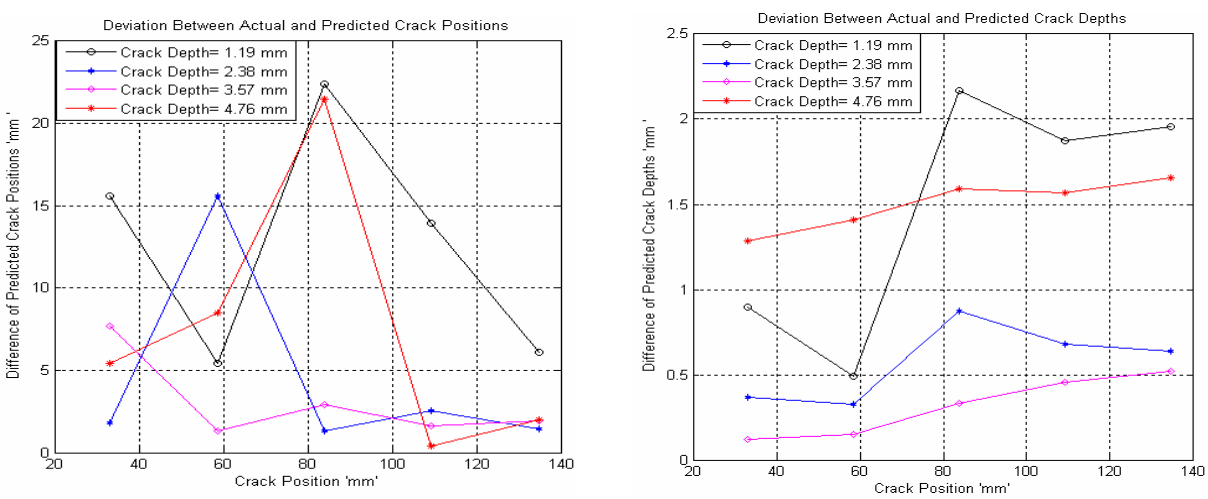

(a) (b)

Figure 43. Performance of the predictor network (a) Crack positions (b) Crack depths

Figure 43 shows a tendency of error reduction in prediction when the crack approaches to the middle of the shaft. This behavior can be attributed to the low sensitivity of the vibration parameters obtained from PSDAA differences obtained from at the nodes of analysis of the structure. Next table summarizes the performance of the selected artificial neural network:

Table 6. Performance of the neural network for experimental data

NEURAL NETWORK PERFORMACE (IN MILIMETERS)					
Average error in positon	Minimal error in position	Maximal error in position	Average error in depth	Minimal error in depth	Maximal error in depth
7.7990	0.3636	26.5853	0.9678	0.1216	2.1658

6.4 Comparison between theoretical and experimental results

Difference between the experimental and theoretical PSDAA are shown in

Table 7. Comparison between theoretical and experimental PSDA

Crack Positions [mm]	Power Spectral Density Differences Between Theoretical and Experimental Results in (g^2/Hz)											
	Crack Depths for Node 4 (Milimeters)				Crack Depths for Node 5 (Milimeters)				Crack Depths for Node 6 (Milimeters)			
	1.19	2.38	3.57	4.76	1.19	2.38	3.57	4.76	1.19	2.38	3.57	4.76
25.4	-3.925424	-4.721831	-6.39486	-7.4235	-3.071822	-5.362959	-5.865995	-7.142771	-2.828065	-4.859844	-5.801755	-6.791561
38.1	-5.271229	-7.370456	-9.559601	-9.737246	-4.434037	-7.103959	-8.568266	-9.21773	-3.867232	-5.626536	-6.14265	-7.379665
50.8	-6.499213	-6.565589	-9.030416	-9.609085	-6.2965	-6.504035	-8.954275	-9.231728	-6.213897	-6.449919	-6.624946	-7.754164
63.5	-8.60539	-9.295917	-8.643425	-8.840988	-8.436717	-8.965466	-9.112119	-9.387387	-8.25128	-8.791012	-9.139241	-10.48889
76.2	-9.74085	-9.815036	-8.706548	-8.49885	-9.363593	-10.39574	-9.924682	-12.05079	-8.021926	-8.476786	-8.479054	-9.404616
88.9	-10.42743	-8.53316	-7.017799	-4.887284	-10.45754	-10.30304	-9.536457	-9.22341	-9.805796	-10.41037	-11.23718	-12.1026
101.6	-10.1509	-7.583684	-3.427432	0.95746	-6.917364	-5.129932	-3.053277	-3.198505	-4.905924	-6.200659	-7.758333	-7.655451
114.3	-10.24869	-6.501484	-0.222513	5.45857	-11.02244	-10.91113	-8.959647	-5.65484	-10.31723	-11.08229	-12.86123	-13.02094
127	-16.07791	-9.091614	-4.406515	1.449949	-18.09372	-14.66119	-14.92334	-12.7063	-15.30817	-15.75888	-16.61874	-18.16559
139.7	-16.87258	-11.34745	-0.301542	10.23585	-19.19223	-14.52632	-12.73987	-8.146211	-17.80837	-21.44047	-24.71216	-28.83914

Last table shows how the differences became higher as the crack is closer to the middle of the shaft where the vibration signal is larger. This behavior could be associated with the plastic deformation of the shaft vibrating close to the critical speed where the deflections and internal stresses are higher.

Table 8. Comparison between theoretical and experimental predicted data

	NEURAL NETWORK PERFORMACE (IN MILIMETERS)					
	Average error in positon	Minimal error in position	Maximal error in position	Average error in depth	Minimal error in depth	Maximal error in depth
Theoretical	7.2119	0.0178	16.8989	0.6578	0.1257	2.0365
Experimental	7.7990	0.3636	26.5853	0.9678	0.1216	2.1658
Difference	0.5871	0.3458	9.6865	0.3099	-0.0042	0.1294

7 Results and conclusions

This study developed a method for online failure diagnosis on a shaft rotating with an unbalance disk at the midspan. A unique pattern of acceleration signals acquired from a new wireless sensor capable of being mounted at different positions of the shaft allow the development of neural network performing as a predictor in order to associate the crack characteristics from the vibration parameters. The selection of the predictor network architecture was based on its performance in pattern recognition. A simulating study was carried out employing the finite element method to model the problem before experimental application. The method was successfully implemented within a degree of accuracy to diagnose the crack depth and position in a rotating shaft demonstrating the effectiveness of the artificial neural networks predictor working in combination with the wireless sensor giving a signal in the rotating coordinates.

Results of the simulating study:

The harmonic force induced by the unbalance disk in the middle of the shaft was derived for the dynamic system considering a single degree of freedom for the rotating coordinate system relative to the wireless accelerometer. Deflection and acceleration equations as a function of the mode shape functions were obtained first analyzing the uncracked shaft for any time and position in the shaft modeling a continuous shaft in bending vibration and then for the cracked shaft by means of the finite element method. The first natural frequency estimated in the mathematical model resulted very close to those estimated with the finite element model employing the consistent mass matrix in stead of the lumped mass matrix.

Conclusions of the simulating study:

Modal parameters such as mode shapes and natural frequencies obtained from the finite element model resulted to be very sensitive to crack depth and crack location.

The differences of PSDAA between the cracked and uncracked shaft at three different positions have shown to be a unique pattern of the failure scenario, except in crack positions close to the shaft support. This unique characteristic was successfully employed as the diagnostic input sensitive parameter to find a function approximator networks able to correlate this pattern with the failure characteristics employing the Backpropagation training algorithm.

Experimental results of simulating data in Table 3 corresponding to the analysis of variance show that the performance of the network predictor depends simultaneously on the number of data, number of neurons and the interaction of both.

A predictive structure revealing the lowest error with the smallest number of neurons was identified from the results of the experiment. A single neuron in the hidden layer was considered working with a sigmoidal transfer function and two neurons with linear transfer functions in the output layer.

Differences in crack position predictions close to the shaft support were found due to the low sensitivity of the vibration parameters obtained from the three points selected.

Results of the experimental study:

A new wireless sensor was designed and fabricated for extracting the vibration signals from a rotating shaft at different positions. The power spectral densities of the acceleration signals were successfully acquired by means of the signal conditioning and signal processing systems developed for the study.

Low signal sensitivity was found when the crack approached to the supports, where the deflections are small.

Acceleration range of the sensor limited the experiment to frequencies lower than the first harmonic increasing the noise amount in the signal.

Conclusions of the experimental study:

Experiment results in Table 5 corresponding to the analysis of variance of the errors in prediction show that the performance of the network predictor depends simultaneously on the number of data, the transfer function, the number of neurons and the interaction of number of data, the transfer function and the number of neurons.

The results of the experiment indicated that the structure revealing the lowest average error with the smallest number of neurons was the one with five neurons in the hidden layer, therefore there

was considered a network with a sigmoidal transfer functions with two neurons and two linear transfer functions in the output layer.

Low sensitivity was found in PSDAA signals for both cases; simulating and experimental work, when the crack approached to the shaft support between 0 - 45 mm affecting the performance of the predictor neural network in this range of crack location. However, increasing the number of data set for training resulted in accuracy of the predictor network.

Possible causes of difference between the theoretical and experimental data results are attributed to plastic deformations due to non elastic behavior of the shaft material when they were under bending vibration condition near the fundamental frequency**.**

The small error differences between actual and predicted data in the simulated and experimental studies demonstrated the consistency of the proposed method in the diagnosis of a failure in the shaft employing wireless sensors and artificial neural networks method in a real system.

8 Future Work

This study can be extended to a closed crack considering the breathing behavior of the crack and assuming the crack as a spring in the FEA model.

More than one crack can be studied, both the shaft and the crack may include different type of cross sections and more than one disk can be added to the model.

Acceleration signals obtained in the rotating coordinates from the wireless accelerometer can be employed to analyze the orbits of the shaft at different locations in order to find additional failure patterns that can improve the method.

Vibration acceleration signals can be obtained at higher frequencies closer to the fundamental frequency increasing the range of acceleration of the sensor in order to reduce noise and increase accuracy.

Knowing the crack location and size, a future forecasting method based on fracture mechanics and fatigue can be developed to estimate the residual amount of time left in the shaft working in real time with the selected network.

References

[1] Adewusi Surajudeen Adedotun, " Detection of a Transverse Crack in a Rotating Shaft Using Wavelet Transform", Thesis of Master of Science in Mechanical Engineering, King Fahd University of Petroleum & Minerals, 233 pages, May 2000.

[2] Alkhalifa Tareq Jawad, " On-Line Damage Detection in Rotating Machinery", Thesis of Doctor of Philosophy in the School of Mechanical, Materials and Aerospace

[3] Analog Devices, Inc, ADXL202E Catalog, at http://www.analog.com,2000.

[4] Bachschmid N., Pennacchi P., Tanzi E. and Vania A., "Identification of Transverse Crack Position and Depth in Rotor Systems", Meccanica, vol 35, pp. 563-582, 2000.

[5] Bikri K. El, Benamar R. and Bennouna M.M., "Geometrically non-linear free vibrations of clamped-clamped beams with an edge crack'', Elservier, Computers and Structures 84, pp. 485-502, 2006.

[6] Demuth Howard Hagan Martin and Beale Mark, "Neural Network Design" , Thompson Learning, Inc., 1996.

[7] Demuth Howard and Beale Mark, ''Neural Network Toolbox for Use with MATLAB'', User's Guide version 3.0, The Mathworks Inc., http://www.mathworks.com, 1998.

[8] Ewins D.J., " Modal Testing Theory and Practice" , Research Studies Press Ltd, 269 pages, 1984.

[9] Fan Yimin and Li C. James, "Nonlinear System Identification Using Lumped Parameter Models With Embedded Feedforward Neural Networks", Rensselaer Polytechnic Institute, 2000.

[10] Feldman Michael & Seibold Susanne, "Damage Diagnosis of Rotors: Application of Hilbert Transform and Multi-Hypotesis Testing", Israel Institute of Technology, 1998.

[11] Gere James M. and Timoshenko Stephen P. "Mechanics of Materials'' ,PWS-KENT Publishing Company, 1990.

[12] Grabowski B., “The Vibrational Behavior of a Turbine Rotor Containing a Transverse Crack", Transactions of the ASME, vol. 102, Jan. 1980.

[13] Haberman Richard ‘’Elementary Applied Partial Differential Equations’’ whit Fourier Series and Boundary Value Problems, second edition by Prentice –Hall, 1987.

[14] Inman Daniel J., “ Engineering Vibration ”, second edition, Prentice-Hall Inc., 2001.

[15] Maharbiz Michael, “Introduction to MEMS – EECS 414 lectures”, Center for Wireless Integrated MicroSystems, University of Michigan, September 2005.

[16] MATLAB Version 7.1.0.246 Release 14, Neural Network Toolbox, The Mathworks Inc., http://www.mathworks.com, August 02, 2005.

[17] McKee Kristoffer K., “Rotor Transverse Crack Detection and Diagnosis Using Embedded Modeling”, Thesis of Doctor of Philosophy in Mechanical Engineering, Rensselaer Polytechnic Institute, Troy, New York, 191 pages, November 2002.

[18] Narkis Y., “Identification of Crack Location in Vibrating Simply Supported Beams’’, Journal of Sound and Vibration, 172(4), pp.549-558, 1994.

[19] Owolabi G.M., Swamidas A.S.J and Seshadri R., “ Crack Detection in Beams Using Changes in Frequencies and Amplitudes of Frequency Response Functions’’, Journal of Sound and Vibration, 263 ,pp1-22,2003 .

[20] Paz Mario, “Structural Dynamics Theory and Computation’’, Van Nostrand Reinhold, Third Edition,626 pages, 1991.

[21] Ramirez Beltran. Nazario, “Neural networks to model dynamic systems with time delays’’, IIE Transactions 34, pp 313-327, 2002.

[22] Sekhar A.S., “Identification of a Crack in a Rotor System Using a Model-based Wavelet Approach”, Technische Universitat Darmstadt, Institute fur Mechanik, 2001.

[23] Sinha Jyoti K., “Bi-spectrum for identifying crack and misalignment in shaft of a rotating machine’’, Smart Structures and Systems, Vol. 2, No. 1, pp. 47-60, 2006.

[24] Tsai T. C. And. Wang Y. Z, “Vibration Analysis and Diagnosis of a Cracked Shaft”, Journal of Sound and Vibration, vol.192, No.3, pp.607-620, 1996.

[25] Xiao Yingming B, “An Experimental Study of Crack Detection in a Rotating Shaft”, Thesis for Master Engineering, Memorial University of Newfoundland-Canada,109 pages, July 1995.

[26] Zill Dennis G. “Ecuaciones Diferenciales con Aplicaciones”, Segunda edición , IberoAmérica, 1988.